

ANALYSIS OF NITROGEN OXIDE EMISSIONS PRODUCED DURING
COMBUSTION OF CRACKED-AMMONIA FUELS

by

Elizabeth Golonski

© Copyright by Elizabeth Golonski, 2024

All Rights Reserved

A thesis submitted to the Faculty and the Board of Trustees of the Colorado School of Mines in partial fulfillment of the requirements for the degree of Master of Science (Chemical Engineering).

Golden, Colorado

Date _____

Signed: _____

Elizabeth Golonski

Signed: _____

Dr. Colin Wolden
Thesis Advisor

Signed: _____

Dr. Douglas Way
Thesis Co-advisor

Golden, Colorado

Date _____

Signed: _____

Dr. Nanette Boyle
Professor and Department Head
Chemical and Biological Engineering

ABSTRACT

Ammonia has emerged as a chemical with the potential to bridge the gap in the global initiative to replace organic fuels with hydrogen. While hydrogen boasts high energy density and zero carbon emissions, it is difficult to store, transport, and utilize directly. Ammonia is a hydrogen-dense chemical that is an excellent hydrogen carrier, thus presenting a means to overcome the storage and transportation challenges associated with hydrogen. Ammonia also provides a means for safe and timely utilization of hydrogen through ammonia-hydrogen combustion. Pure ammonia is difficult to ignite and burn. In contrast, pure hydrogen is extremely flammable and difficult to control. However, ammonia-hydrogen blends have proven to burn efficiently in a myriad of combustion-based power generation systems including gas turbines, compression engines, and spark ignition engines. An advantage of ammonia is that it can produce ammonia/hydrogen blends directly through cracking, which is the decomposition of ammonia to produce hydrogen and nitrogen.

Conventional ammonia cracking produces $\text{NH}_3/\text{H}_2/\text{N}_2$ fuel mixtures. Our research group has developed a catalytic membrane reformer that rejects nitrogen, and produces NH_3/H_2 blends. To date, little attention has been paid to the potential differences of the two blends in terms of combustion. This work compares the flame stability and NO_x production of the two mixtures (with and without additional nitrogen). The range of operating conditions (equivalence ratio, fuel-hydrogen mole fraction, axial velocity) at which laminar burner-stabilized flames exist is defined. Experimental NO_x measurements are compared to Chemkin simulated NO_x concentrations, revealing the potential occurrence of selective catalytic reduction.

In this work we built a laminar, 1-dimensional flat flame apparatus to study NO_x emissions produced from the two mixtures. It was found that rejection of nitrogen improved flame stability, particularly at low fuel-hydrogen mole fractions. However, rejection of nitrogen has negligible effect on the production of NO_x . Initial experiments contradicted expectations based on theoretical modeling in terms of NO_x production. It was determined that the NO_x analyzers used do not function properly in the high humidity environments resulting from ammonia combustion. This issue was partially resolved by providing additional dilution to the post flame sampling region. Under these conditions, very good qualitative agreement between data and model expectations were observed. However, the experimental NO_x concentrations remained below model expectations, which was attributed in part to catalytic reduction of NO_x in the sampling line. This might be a promising avenue for NO_x reduction in the future.

TABLE OF CONTENTS

ABSTRACT.....	iii
LIST OF FIGURES.....	vi
LIST OF TABLES	viii
LIST OF SYMBOLS	ix
LIST OF ABBREVIATIONS	x
ACKNOWLEDGMENTS.....	xi
CHAPTER 1 INTRODUCTION.....	1
1.1 Production, Storage, Transportation, and Utilization of Hydrogen	1
1.2 Potential of Ammonia as both a Hydrogen Carrier and Carbon Free Fuel.....	2
1.3 History of Ammonia use in Combustion Based Applications	6
1.4 Ammonia Combustion: Mechanisms and Predictions	7
1.4.1 Accepted Trends in Ammonia Combustion Mechanisms	7
1.4.2 Nitrogen Oxide Formation in Ammonia Combustion.....	10
1.4.3 Ammonia Slip.....	15
1.4.4 Summary of Ammonia Combustion Trade-offs.....	16
1.5 Hydrogen-Promoted vs. Cracked Ammonia Fuel Mixtures.....	17
1.6 Goals of this Thesis Work.....	19
CHAPTER 2 MATERIALS AND METHODS	21
2.1 Materials	21
2.2 Experimental Design.....	26
2.3 Theoretical Modeling.....	30
CHAPTER 3 RESULTS AND DISCUSSION.....	35
3.1 Flat Flame Operating Conditions.....	35
3.2 NO _x Measurements	39
3.2.1 Model Predictions.....	39
3.2.2 Experimental Results.....	40
3.2.3 Challenges in Experimentation.....	42
CHAPTER 4 CONCLUSIONS AND RECOMMENDATIONS	49
4.1 Conclusions.....	49

4.1.1	Flame Stability.....	49
4.1.2	NO _x Production.....	49
4.2	Recommendations.....	50
REFERENCES		51
APPENDIX A EXPERIMENTAL SPECIFICATIONS.....		54
APPENDIX B CHEMKIN INPUTS.....		58
APPENDIX C PYTHON SCRIPT FOR GOLDMAN'S CORRELATION EQUATIONS		60
APPENDIX D PERMISSIONS		78

LIST OF FIGURES

Figure 1.1	Gravimetric and volumetric hydrogen density of potential hydrogen carriers. Reprinted from Ref. [5], with permission from Elsevier.	3
Figure 1.2	Hydrogen production, transport, and utilization schematic. Reprinted from Ref. [5], with permission from Elsevier.....	3
Figure 1.3	Empirical correlation and measured ignition delay times of NH ₃ /H ₂ mixtures at pressures of 1.2 and 10 atm. Reprinted from Ref. [15] with permission from Elsevier.....	8
Figure 1.4	The relationship between laminar burning velocity with initial fuel mixture pressure at equivalence ratios of (a) 0.9, (b) 1.0, and (c) 1.2. Reprinted from Ref. [12] with permission from Elsevier.....	8
Figure 1.5	Laminar flame speeds for NH ₃ /air mixtures as a function of equivalence ratio at 1 bar and 298 K. Reprinted from Ref. [13] with permission from Elsevier.....	9
Figure 1.6	Laminar flame speeds for NH ₃ /H ₂ fuel mixtures at stoichiometric conditions with fuel-hydrogen mole fraction ranging from 0.0-1.0. Reproduced from Ref. [13] with permission from Elsevier.....	10
Figure 1.7	Emission characteristics in terms of equivalence ratio at 1 bar and 40 mm downstream of the position of maximum heat release rate: (a) NH ₃ /air; (b) CH ₄ /air. Reprinted from [5] with permission from Elsevier.	11
Figure 1.8	NO _x concentrations for stoichiometric NH ₃ /H ₂ /air mixtures as a function of fuel-hydrogen mole fraction at 1 bar and 298 K. Reprinted from Ref. [12] with permission from Elsevier.	12
Figure 1.9	Reaction flow diagram of fuel rich ammonia/air flame at 0.1 MPa in the downstream region of the flame. Reprinted from reference [20]with permission from Elsevier.	15
Figure 1.10	Laminar burning velocity profiles of (a) NH ₃ /H ₂ /Air flames and (b) NH ₃ /H ₂ /N ₂ /Air flames across a range of equivalence ratios from 0.5-1.9 and fuel-hydrogen mole fractions from 0.0-0.5.....	18
Figure 1.11	Variations of NO _x (NO, NO ₂ and N ₂ O) for various compression ratios. Reprinted from reference [24] with permission from Elsevier.....	18
Figure 1.12	(a) Comparison of NO _x emissions with NH ₃ /H ₂ /N ₂ fuel reprinted from Ref. [27] with permission from Elsevier, and (b) NO _x emissions with NH ₃ /H ₂ fuel, $\phi = 1.0$, reprinted from Ref. [25] with permission from Elsevier.	19
Figure 2.1	(a) Photograph of the vacuum chamber, (b) photograph of the inside of the chamber, and (c) process flow diagram of the apparatus employed in this work.....	22
Figure 2.2	(a) Photograph and (b) schematic diagrams of burner interior. Reprinted from [28]with permission from Leneke Holthuis.	23
Figure 2.3	(a) NO _x analyzer, (b) Analyzer process flow diagram. Images from ECO Physics user manual [29]. Reprinted with permission from ECO Physics.	25
Figure 2.4	Photographs of H ₂ /NH ₃ flat flames ranging from 70% H ₂ on the left to 20% on the right in 10% increments. The ideal flat flame condition is lost in the last 2-3 images. Reprinted from Ref. [30], an open source presentation.	26

Figure 2.5	Experimental inlet fuel/oxidizer velocity (cm/s) and calculated laminar flame speed for fully developed flames for $0.x_{H_2}$ ranging from 15-50% and 9.67-42.9% for (a) NH_3/H_2 and (b) $NH_3/H_2/N_2$ fuel mixtures respectively.....	28
Figure 2.6	Configuration for sampling the exhaust gas.....	30
Figure 2.7	PREMIX simulation schematic in Chemin with an inlet source, non-reactive mixer, premixed laminar burner-stabilized flame, and outlet flow models (from left to right).....	31
Figure 2.8	Fuel/oxidizer velocity fed to the burner (experimental, Exp) compared to the LBV at the burner surface upon ignition (Chemkin) for NH_3/H_2 and $NH_3/H_2/N_2$ mixtures at $\phi = 1.0$	32
Figure 2.9	Flame profile for 30% H_2 , NH_3/H_2 fuel mixture at $\phi = 1.0$ with (a) major species (NH_3 , H_2 , O_2 , H_2O) and temperature and (b) the major impurities including critical NO_x emissions, NH_3 slip, and persistent radicals H and OH.....	34
Figure 3.1	Flame profiles for $\phi = 0.8$ and 0.9	36
Figure 3.2	Flame profiles for $\phi = 1.0$ and 1.1	37
Figure 3.3	Model predictions NO_x concentration 15mm above the burner surface at $\phi = 1.0$, varying x_{H_2}	39
Figure 3.4	Model predictions of NO_x concentration for 30% hydrogen fuel mixtures as a function of equivalence ratio 15mm above the burner surface.	40
Figure 3.5	Average experimental NO_x concentrations of NH_3/H_2 mixtures compared to $NH_3/H_2/N_2$ mixtures at (a) $\phi = 0.8$, (b) $\phi = 0.9$, and (c) $\phi = 1.0$ as a function of x_{H_2}	41
Figure 3.6	NO_x measurements of experimental (Exp) results compared to Chemkin (C) results for $x_{H_2} = 0.3$	42
Figure 3.7	NO_x analyzer calibration gas measurements pre and post combustion operations.....	43
Figure 3.8	NO_x detector and NO_x analyzer sample tube location with emphasis on the detection and sample tube locations.	45
Figure 3.9	Comparison of NO_x measurements between the NO_x analyzer and NO_x detector across the range of operating conditions for the NH_3/H_2 mixture, with chamber ventilation.	46
Figure 3.10	Comparison of NO_x emissions between NH_3/H_2 and $NH_3/H_2/N_2$ flames with NO_x analyzer and chamber ventilation.....	47
Figure 3.11	NO_x measurements of experimental (Exp) results compared to Chemkin (C) results for $x_{H_2} = 0.3$	48
Figure 3.12	Comparison of model predictions and experimental results of NO_x for $\phi = 1.0$, $x_{H_2} = 0.15-50$ for both NH_3/H_2 and $NH_3/H_2/N_2$ mixtures.	48

LIST OF TABLES

Table 1.1	Hydrogen content and volumetric energy densities of common fuels. Modified from Ref. [2] with permission from Elsevier.....	2
Table 1.2	Combustion Characteristics of ammonia and common hydrocarbon fuels. Modified from Ref. [2] with permission from Elsevier.....	4
Table 2.1	Calculations and methodology for experimental flow rates.....	27
Table 3.1	Flammability ranges of NH ₃ /H ₂ and NH ₃ /H ₂ /N ₂ mixtures at various equivalence ratios	38
Table A.1	Component Volumetric flow rates (SLM) used for NH ₃ /H ₂ and NH ₃ /H ₂ /N ₂ mixtures, across the range of operating conditions ($\phi = 0.8-1.1$, $x_{H_2} = 0.10-0.50$).....	54
Table B.1	Entries for the Chemkin Premixed Burner Code for $\phi = 1.0$	58
Table B.2	Chemkin Outputs for Adiabatic Flame Temperatures using the Equilibrium Code for $\phi = 1.0$	58
Table B.3	Chemkin “Solve Gas Energy Equation” Parameter Values	59

LIST OF SYMBOLS

Equivalence ratio	ϕ
Laminar Burning Velocity	S_L
Volumetric flow rate	Q
Fuel-hydrogen mole fraction	x_{H_2}

LIST OF ABBREVIATIONS

Equivalence Ratio	ER
Laminar Burning Velocity	LBV
Laminar Flame Speed	LFS
Standard Cubic Centimeters per Minute	Scm
Selective Catalytic Reduction	SCR
Selective Non-Catalytic Reduction	SNCR
Standard Liter per Minute	SLM

ACKNOWLEDGMENTS

I would like to thank my research advisor, Dr. Colin Wolden, for his diligent mentorship throughout my re-entry into academia and introduction into research. This work would not have been possible without his patience and guidance. My gratitude extends to my research co-advisor (Dr. Douglas Way), and my M.S. Thesis committee (Dr. Sumit Agarwal and Dr. Stephanie Kwon) for their time and attention in the pursuit of this research. My deepest thanks also go to my former peer, Dr. Rok Sitar, and current peer, Nolan Kelley for their assistance throughout this research. I especially appreciate Isabelle Roszelle for her diligent completion of experiments. This work was made possible thanks to the generous funding of ARPA-E that enabled the purchase of equipment and materials. Finally, I would like to thank the Army and especially the United States Military Academy for affording me the opportunity to pursue this degree.

1.1 Production, Storage, Transportation, and Utilization of Hydrogen

There is a global initiative to develop reliable, carbon-free energy sources to diminish dependence on fossil fuels and reduce CO₂ emissions. Researchers and industries have explored the use of renewable sources such as solar, wind, and geothermal; all of which are intermittent forms of energy that require accumulative storage to meet daily demands. Unfortunately, replacing combustion-based energy systems with renewable energy sources in the near term is not feasible [1], [2]. Thus, much focus is on developing an alternative fuel source to directly replace hydrocarbons in combustion-based power generation systems.

Hydrogen has emerged as the most popular carbon-free fuel given its high specific energy and water being its primary byproduct. At present, the overwhelming majority (>90%) of hydrogen is produced by steam reforming of hydrocarbons, which is energy intensive and releases more than 10 kg CO₂ per kg H₂ [3]. However, there are alternative hydrogen production methods and they are categorized in terms of color (blue, white, green). Blue hydrogen is used to describe conventional hydrogen production that is coupled with the capture and sequestration of the co-generated CO₂. White hydrogen is naturally occurring and has attracted interest recently but remains in the early stages of development [4]. Green hydrogen is produced through the electrolysis of water using renewable electricity, and in this case can have an exceptionally low carbon-footprint [2]. With the focus on climate change, paired with wind and solar being the fastest growing sources of primary power, it is expected that the availability of low carbon hydrogen (green/blue/white) should increase dramatically in the coming decades.

However, widespread utilization of hydrogen is constrained by additional challenges. The first challenge is efficient storage and transportation. Gaseous hydrogen has a very low volumetric energy density and requires liquefaction and/or extreme compression. These energy intensive processes require cryogenic temperatures (-252.9 °C) or extreme pressure (>700 bar), which diminish the energy value of this resource [3], [5]. Moreover, the extreme volatility of hydrogen leads to boiloff and loss. At scale this also presents a significant safety challenge due to its very low ignition energy and flammability limit (~4%) [6].

The second issue is its efficient utilization. Much attention has been paid to hydrogen fuel cells which convert hydrogen back into electricity, but they are complicated devices that employ expensive materials and have a relatively limited footprint in the energy economy. A much greater opportunity is direct combustion processes such as process heating, gas turbines, and internal combustion engines. However, the extreme flame speed and temperature of hydrogen make it particularly challenging to control and use directly in conventional combustion-based applications.

1.2 Potential of Ammonia as both a Hydrogen Carrier and Carbon Free Fuel

Enter ammonia (NH₃): a hydrogen-dense chemical that addresses the challenges associated with the storage, transport, and utilization of hydrogen. Ammonia is liquid at room temperature and modest pressure (1/87th the pressure required for liquid hydrogen) [2]. Figure 1.1 compares the gravimetric hydrogen density and volumetric energy densities of ammonia, common hydrocarbons, and hydrogen, pointing out that ammonia has the highest volumetric H₂ density. Table 1.1 presents the case for ammonia: it has the highest hydrogen content by weight percent and its volumetric energy density is 2.3 times higher than that of hydrogen. Additionally, production and distribution of ammonia is already well established. Over 200 million metric tons (MMT) of ammonia are produced annually for a range of applications, such as fertilizer, cleaning solution, refrigerant, food preservative, and emission controller in the auto industry [5], [7]. Transportation of ammonia is already established due to its existing footprint. Transport mechanisms used for propane can readily accommodate ammonia since their boiling temperature and condensation pressures are quite similar (-33.4 °C and 9.90 atm for ammonia, -42.1 °C and 9.40 for propane) [5]. Although ammonia is toxic in high concentrations, leaks are easily detected due to its pungent odor. Safety precautions regarding its handling and use are well established. Perhaps its most attractive feature is that ammonia is a carbon-free fuel, and complete combustion of NH₃ produces water and nitrogen.

Table 1.1 Hydrogen content and volumetric energy densities of common fuels. Modified from Ref. [2] with permission from Elsevier.

Fuel	H ₂ content (wt%)	Volumetric energy density (Wh/L)
Ammonia	17.7	4325
Methanol	12.5	4600
Ethanol	13	6100
Gasoline	15.8	9700
Hydrogen	100	1305

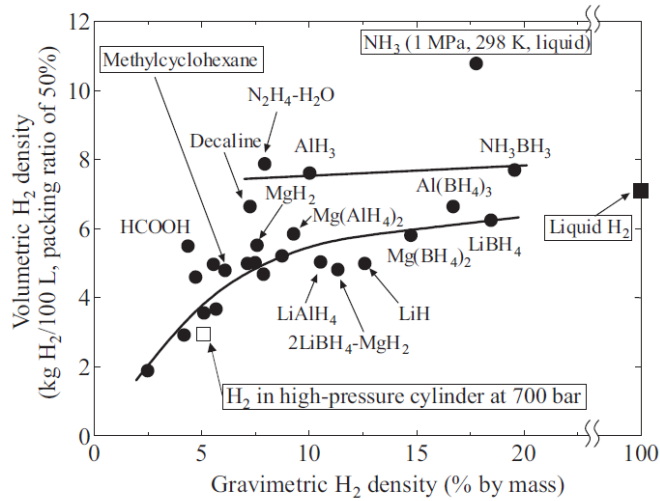


Figure 1.1 Gravimetric and volumetric hydrogen density of potential hydrogen carriers. Reprinted from Ref. [5], with permission from Elsevier.

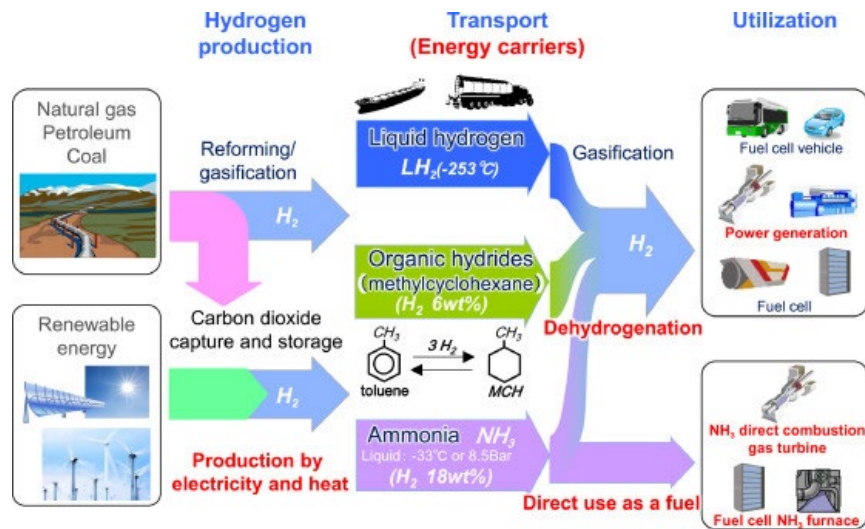


Figure 1.2 Hydrogen production, transport, and utilization schematic. Reprinted from Ref. [5], with permission from Elsevier.

Figure 1.2 provides a schematic of how ammonia fits into a larger goal to establish a hydrogen-economy. Produced hydrogen can be efficiently and practically “carried” by ammonia. That ammonia can then either be dehydrogenated for direct hydrogen use, or applied directly as a fuel into combustion-based power generation systems or fuel cells. Compared to organic hydrides, ammonia contains three times as much hydrogen by weight percent. As discussed previously, transporting liquid hydrogen is expensive and requires high pressures or extremely low temperatures. Ammonia presents itself as a promising

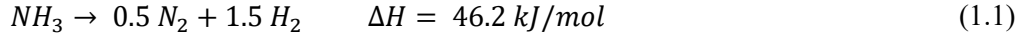
option for chemically storing hydrogen and direct use as a hydrogen-dense fuel. Subsequently, researchers have explored the potential of using ammonia in lieu of hydrocarbon fuels.

Despite the multiple benefits inherent with ammonia, disadvantages become apparent in its combustion characteristics, compared in Table 1.2. While a dense hydrogen carrier, its energy density is ~2.5 times less than conventional hydrocarbons. Its low burning velocity (~7 cm/s) makes it difficult to maintain stable combustion. Hydrogen is at the other extreme (~291 cm/s), making hydrogen flames very difficult to control. Combustion devices have been designed to work at hydrocarbon flame speeds (30-50 cm/s), making neither pure ammonia nor pure hydrogen ideal for direct application. Unlike hydrogen, ammonia has a high ignition energy, a very low speed, and a much smaller flammability range, which is favorable from a safety perspective, but complicates ignition.

Table 1.2 Combustion Characteristics of ammonia and common hydrocarbon fuels. Modified from Ref. [2] with permission from Elsevier.

Fuel	NH ₃	H ₂	CH ₄	C ₃ H ₈
Calorific value (MJ/kg)	18.6	120	50	46.4
Maximum laminar burning velocity (m/s)	0.07	2.91	0.37	0.43
Flammability limit (Equivalence ratio)	0.63-1.4	0.10-7.1	0.50-1.7	0.51-2.5

Fortunately, research has demonstrated multiple techniques to mitigate or overcome the disadvantages of direct ammonia combustion. The most direct is to add an accelerant such as H₂, thereby producing fuel blends with improved combustion efficiency and characteristics compared to neat ammonia. However, storing additional hydrogen remains a key problem. A promising solution is through partial ammonia decomposition, also known as ammonia cracking, where hydrogen is obtained through the decomposition of ammonia in the presence of a solid catalyst [8]. Ammonia cracking is an endothermic reaction that demonstrates as high as 99% conversion with appropriate catalyst and operating conditions (Equation 1.1). This reaction presents a means to produce ammonia-hydrogen fuel blends, which are far more compatible than neat hydrogen or neat ammonia in existing combustion systems.



NH₃ decomposition occurs through a thermochemical reaction consisting of three steps: NH₃ adsorption into the metal catalyst; NH₃ dehydrogenation; and desorption of H₂ and N₂ from the catalyst. The reaction requires a large amount of heat to reach the optimal reaction temperature of 350-900 °C depending on the catalyst and operating pressure. The most common catalysts for NH₃ cracking include ruthenium (Ru), nickel (Ni), iron (Fe), and copper (Cu), listed in descending order of activity. Ru catalysts are the most reactive, while Ni is used commercially due to its low cost. Often the metal is impregnated into a porous support material such as metal oxides, carbon nano tubes, graphitic carbon, and active carbon, which are often employed to increase the electronic density of the catalysts' active sites. Similarly, catalysts' surfaces can be modified with promoters such as potassium (K), sodium (Na), or calcium (Ca) to improve the adsorption energy of nitrogen, thereby enhancing the breakage of hydrogen-nitrogen bonds and improving the overall conversion [9].

Ammonia cracking can take place in multiple reactor types. Conventionally the most common approach is to conduct decomposition in packed bed reactors (PBR). With a commercial Ni catalyst this requires temperatures of 800 °C for complete decomposition, though it can be reduced below 500 °C with Ru. Decomposition produces forming gas (H₂/N₂), and purification requires compression followed by pressure swing adsorption (PSA). This is a well-established process, but is both capially and operationally expensive.

Packed bed membrane reactors (PBMR) combine reaction and separation in one process intensified unit operation. They are used when separating the products and unburned reactant is desired. PMBRs have proven to be excellent for separating the reaction components, with selectivity ratios for H₂/NH₃ of 200, and H₂/N₂ of 720, resulting in nearly pure hydrogen in the permeate stream. PBMRs also have the benefit of improving the space velocity by 20% compared to PBRs, reducing the reaction temperature by up to 400 °C. PBMRs demonstrate modest improvements in NH₃ decomposition but have transport limitations that restrict their effectiveness [10]. After hydrogen atoms desorb from an individual catalyst pellet, they must then diffuse radially through the reactor bed and support membrane before transporting away in the permeating flow. Reducing pellet size mitigates the limitations of the transport mechanisms.

Zhang et. al developed a catalytic membrane reformer (CMR) that overcomes some of the transport limitations inherent in PBRs and PBMRs. The membrane in a CMR is both catalytically active and permselective, allowing hydrogen desorption to occur adjacent to the permeable membrane. Therefore, the length scale of diffusive transport is reduced from millimeters to microns. The researchers used a Ru catalyst dispersed on yttria-stabilized zirconium (YSZ), with a cesium (Cs) promoter. The catalyst was impregnated onto a porous oxide support prior to the application of a palladium (Pd) membrane by

electroless deposition. They demonstrated the effectiveness of the Cs promoter across a range of ammonia flow rates. The CsRu CMR reached 93% conversion at 400 °C, and 26% conversion at 350 °C compared to 31% and 400 °C and 8% at 350 °C for the Ru CMR without the Cs promoter [10].

A further advancement in using CMRs for ammonia cracking was proposed by Sitar et. al. They demonstrated the use of an ammonia sweep gas in conjunction with a CMR to produce customizable NH₃/H₂ blends. The use of the NH₃ sweep stream dilutes the hydrogen concentration in the permeate stream, thus increasing the pressure driving force across the membrane. Hydrogen recovery increased by 6-20% at 450 °C, and by more than 69% at 350 °C. An exciting feature of this CMR is that the hydrogen composition in the permeate can be adjusted by controlling the sweep gas flow rate. This development provides an all-in-one mechanism to produce NH₃/H₂ fuel blends composed of 0-99% hydrogen [11]. Typically, membrane reactors require the use of a pressure differential to extract the product (in this case H₂). Another benefit of using a sweep gas is that the CMRs may be operated isobarically, and these H₂/NH₃ blends may be generated at elevated pressure without compression. This is a critical attribute that helps overcome the intrinsic lower energy density relative to hydrocarbon fuels. A final important attribute of the CMR is the rejection of N₂, which increases the specific calorific value of the blends.

1.3 History of Ammonia use in Combustion Based Applications

As early as 1949, ammonia was tested as an alternative to fossil fuels in transportation vehicles [8]. Later in 1965, Samuelsen investigated ammonia/air flames in spark ignition engines, finding that ammonia has a slower flame propagation rate than iso-octane fuel [1]. Within the same decade, NASA used liquid ammonia and liquid oxygen to power its X-15 rocket-powered airplane, which set a world record for the highest Mach number for a manned flight of 6.7 [5]. Shortly after, Bull determined that ammonia could replace hydrocarbon-fuels in select industrial gas turbine engines, however at a fuel consumption rate 2.25 times higher than that of hydrocarbons for the same power output [7]. Studies have concluded that ammonia is challenging to use directly as a fuel. There was little pursuit of ammonia as a fuel for combustion systems throughout the 1970s and 1980s. But a renewed interest in the 1990s brought ammonia back to prominence as a potential way to address climate change. Since then, research into ammonia utilization for combustion engines and gas turbines has become a large area of interest [5].

Despite less-than-ideal combustion characteristics, the carbon-free nature of ammonia and its proven compatibility with multiple combustion systems makes it an attractive fuel source. Japanese energy organizations have identified ammonia as one of the most promising hydrogen carriers, and dedicated multiple projects to using ammonia in gas turbines, reciprocating engines, industrial furnaces, and coal combustion for generating power [5]. The potential for using ammonia in gas-powered turbines is feasible

when blended with promoters, such as hydrogen or methane. Actual demonstrations of ammonia producing energy in micro gas turbines, swirl combustors, micro burners, spark-ignition engines, and compression-ignition engines have been conducted [5], [7], presenting ammonia as an alternative fuel that can be incorporated into the energy economy within a near-term timeframe.

1.4 Ammonia Combustion: Mechanisms and Predictions

The combustion of ammonia follows the global reaction in Equation 1.2:



Chemical reaction mechanisms for ammonia combustion have been under development for over 60 years and continue to be refined. Alnasif's review of the current mechanisms available in the literature reveals that no singular mechanism sufficiently predicts the laminar flame speed, ignition delay time, and nitrogen oxide emissions of ammonia flames simultaneously. Agreement with experimental data across a wide range of equivalence ratios (ϕ), temperatures, pressures, and mixing ratios has not been achieved. For example, Duynslaegher's mechanism accurately predicts laminar flame speed under lean and stoichiometric conditions but fails to converge on experimental NO mole fraction data. Similarly, models proposed by Mathieu and Petersen successfully reproduce experimental ignition delay times in shock tubes but overestimate laminar flame speed of ammonia (A et al., 2023). The largest disparities in the mechanisms are with respect to NO mole fractions, where there is a lack of consensus regarding the most influential kinetic reactions involved in the formation and consumption of NO.

1.4.1 Accepted Trends in Ammonia Combustion Mechanisms

There are four general trends that NH₃ combustion mechanisms agree upon: (1) operating at high temperature and elevated pressure decreases ignition delay timing; (2) combustion at elevated pressure slightly decreases laminar burning velocity [12]; there is a bell-curve relationship between fuel/air equivalence ratio and laminar burning velocity [6], [12], [13]; (3) ammonia's relatively low flame speed and thick flame structure render ammonia flames susceptible to combustion instabilities such as engine knock and spontaneous extinction [14]; and (4) the demonstration that the aforementioned inferior combustion characteristics can be mitigated or overcome by co-firing ammonia with more combustible gasses [8].

Ammonia is difficult to ignite, requiring 16 times the minimum ignition energy as propane (8 mJ at $\phi=0.9$, vs 0.5 mJ for propane) [2]. However, Figure 1.3 shows that preheating ammonia and operating at elevated pressure reduces ignition delay time significantly. Furthermore, adding hydrogen enables faster ignition at lower temperatures [15].

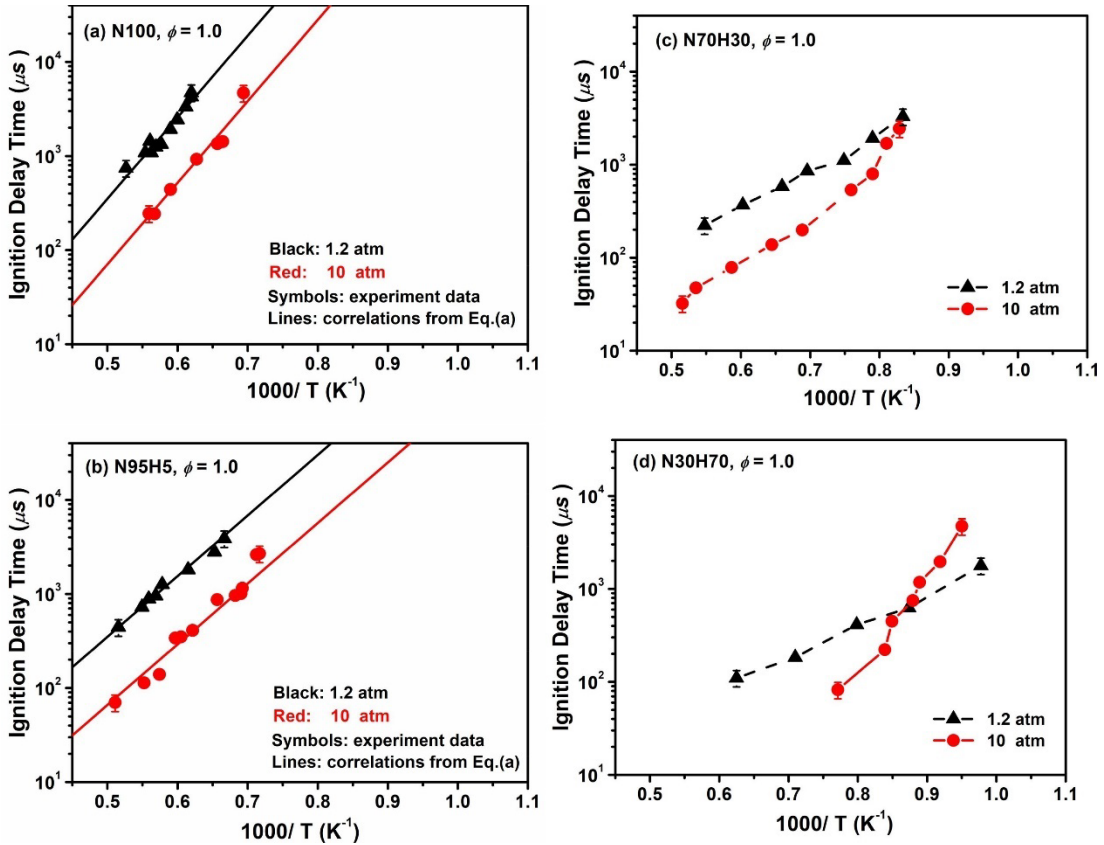


Figure 1.3 Empirical correlation and measured ignition delay times of NH_3/H_2 mixtures at pressures of 1.2 and 10 atm. Reprinted from Ref. [15] with permission from Elsevier.

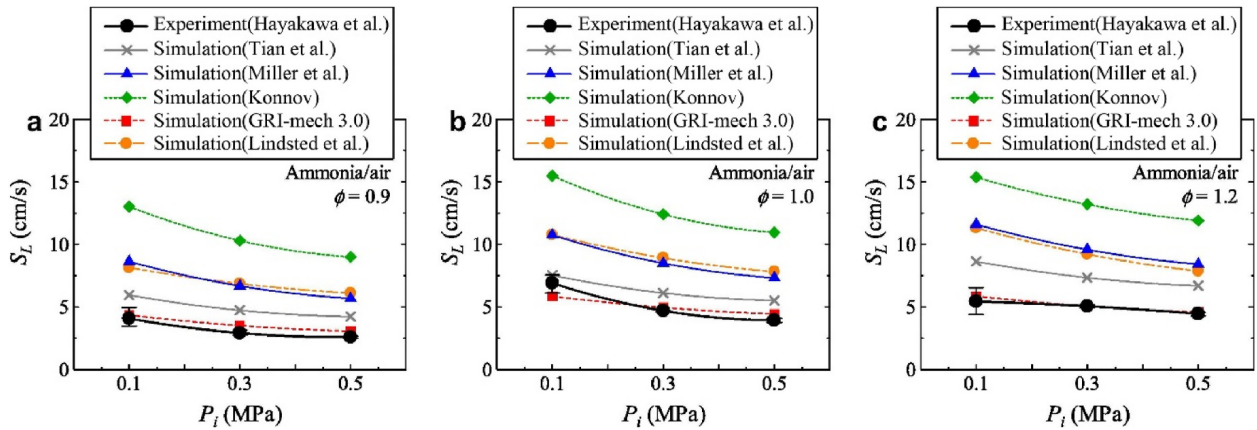


Figure 1.4 The relationship between laminar burning velocity with initial fuel mixture pressure at equivalence ratios of (a) 0.9, (b) 1.0, and (c) 1.2. Reprinted from Ref. [12] with permission from Elsevier.

Figure 1.4 displays the relationship between laminar burning velocity (LBV, S_L) and pressure in lean, stoichiometric, and rich conditions for neat ammonia combustion. Operating at high pressure slightly reduces LBV, which reduces combustion efficiency and power generation.

Multiple mechanisms accurately predict that laminar burning velocity for neat ammonia combustion is maximized at a fuel/air equivalence ratio of ~ 1.1 , whereas lean and rich conditions have slower flame propagation (Figure 1.5).

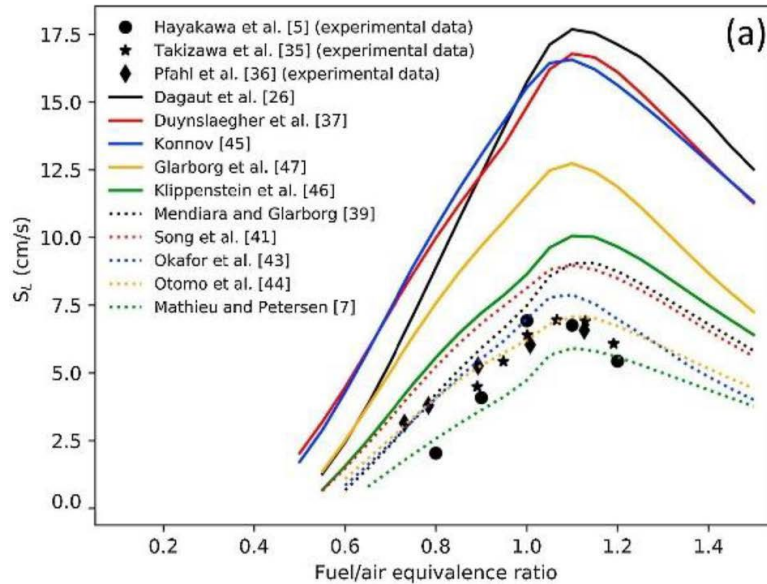


Figure 1.5 Laminar flame speeds for NH_3/air mixtures as a function of equivalence ratio at 1 bar and 298 K. Reprinted from Ref. [13] with permission from Elsevier.

The combustion characteristics of ammonia mixed with promoters such as hydrogen or methane is a primary focus in the field. Mixing either with ammonia has the benefit of reducing ignition delay and increasing flame speed [12]. However, introducing methane inevitably prolongs the problem of carbon emissions. Thus, much focus has shifted on refining kinetic reaction mechanisms for NH_3/H_2 fuel mixtures. Even a modest addition of hydrogen of 8% by volume enhances laminar burning velocity enough to enable continuous engine performance [8]. There is consensus across a range of models that increasing fuel-hydrogen mole fraction increases laminar burning velocity exponentially due to the high reactivity of hydrogen (Figure 1.6). The laminar burning velocity of NH_3/H_2 mixtures is comparable to that of CH_4/air mixtures when $x_{\text{H}_2} \approx 0.4$ [5]. However, estimating NH_3 oxidation in majority-ammonia fuels has proven challenging due to the third body effects caused by ammonia. Despite recent improvements in the accuracy of NH_3 kinetic models and a general understanding of NH_3 combustion and blends thereof, Alnasif et al. identified a need for accurate experimental measurements across a range of

operating conditions especially mechanisms that incorporate hydrogen oxidation sub-mechanisms require further improvements [13].

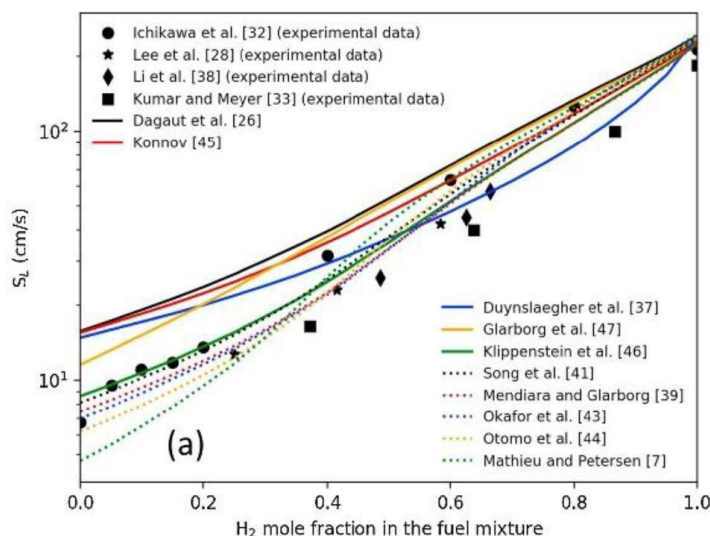


Figure 1.6 Laminar flame speeds for NH_3/H_2 fuel mixtures at stoichiometric conditions with fuel-hydrogen mole fraction ranging from 0.0-1.0. Reproduced from Ref. [13] with permission from Elsevier.

1.4.2 Nitrogen Oxide Formation in Ammonia Combustion

While low laminar burning velocity and high minimum ignition energy of ammonia combustion can be overcome by adding promoters, doing so comes at the cost of increasing nitrogen oxide (NO_x , consisting of NO , NO_2 , and N_2O), a regulated pollutant that results from oxidation of the nitrogen in the fuel or the air. Thus, investigating the formation pathways of NO_x has become a prominent area of study. The majority of emissions-based studies focus on examining nitric oxide (NO) due to experimental mole fraction values being three orders of magnitude larger than that of other nitrous oxides (NO_2 and N_2O). Compared to CH_4/air flames, NH_3/air flames emit more than ten times as much NO in fuel lean mixtures (Figure 1.7). However, under rich conditions the rate of NO production in NH_3/air flames decreases faster than the NO generated from the CH_4/air flames as the equivalence ratio increases. Figure 1.7 demonstrates that at equivalence ratios ≥ 1.05 , NO produced from NH_3/air flames decreases to 10-100 ppm, within the range of CH_4/air flames, with the added benefit of zero carbon-based emissions, further making the case for investigating ammonia as an alternative fuel [12]. However, operating at a higher equivalence ratio also increases the mole fraction of unburnt ammonia. Hence, there is a trade-off between NO and unburnt NH_3 concentrations that needs to be optimized before implementing ammonia as a fuel at scale.

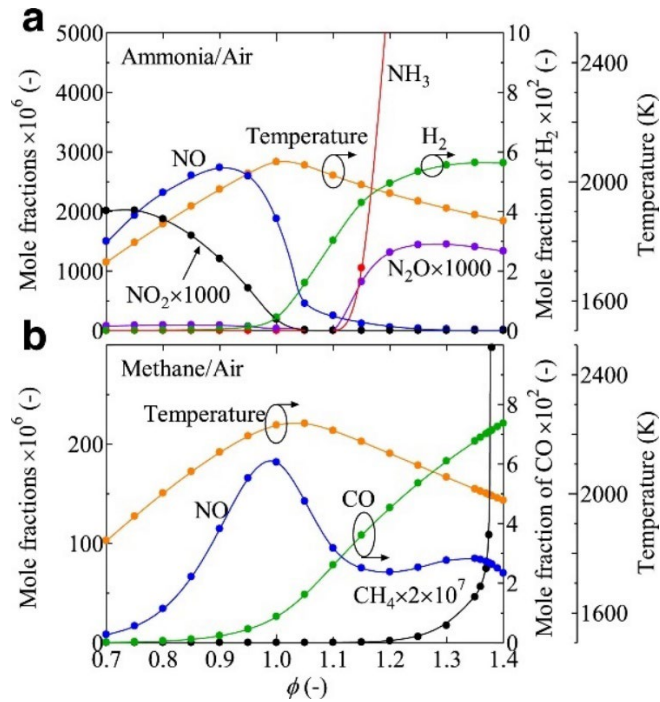


Figure 1.7 Emission characteristics in terms of equivalence ratio at 1 bar and 40 mm downstream of the position of maximum heat release rate: (a) NH₃/air; (b) CH₄/air. Reprinted from [5] with permission from Elsevier.

NO_x emissions are also profoundly impacted by the presence of additional hydrogen in the fuel. Figure 1.8 compares NO_x concentrations at stoichiometric conditions for NH₃/H₂/air blends as a function of fuel-hydrogen mole fraction (x_{H_2}), demonstrating an increase in hydrogen content increases NO_x emissions [12]. Though all models agree on the overall trend, another important point of Fig. 1.8 is the significant disagreement among these in absolute NO_x level. So, while increasing x_{H_2} is beneficial in terms of reducing ignition delay timing, increasing laminar burning velocity, and promoting flame stability, the negative impact of increasing NO_x emissions potentially outweighs the benefits. The range of x_{H_2} values where the tradeoff is mitigated, i.e. where the combustion characteristics are improved and NO_x emissions are within an acceptable range, has yet to be defined in the literature.

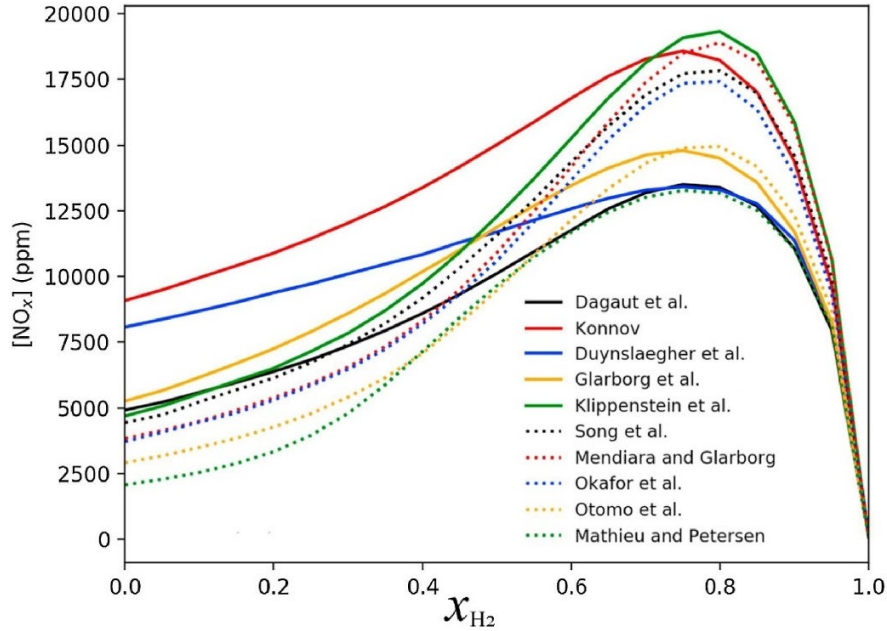


Figure 1.8 NO_x concentrations for stoichiometric NH_3/H_2 /air mixtures as a function of fuel-hydrogen mole fraction at 1 bar and 298 K. Reprinted from Ref. [12] with permission from Elsevier.

NO_x emissions vary based on the type of the combustion device (i.e. engine/burner/turbine) as well as the specific conditions such as fuel-to-air equivalence ratio (ϕ), pressure, and the presence of a promoter (such as hydrogen or hydrocarbons) [16]. In fuel-lean conditions, oxygen radicals attack ammonia to produce NH_2 and OH . Subsequently, NO is formed from HNO , NH , and N radicals, while N_2O is formed from NH radicals attacking NO [7]. In fuel-rich conditions, oxygen and hydrogen radical concentrations decrease due to lower oxygen concentrations in the fuel. Yet at the same time, the proportion of hydrogen radicals to oxygen radicals increases. This proportionality increase causes an enrichment in hydrogen radical concentration and leads to a higher tendency for NH_x radicals to combine with H and to be oxidized. NH_x is also oxidized through a self-bonding reaction. Thus, NO production decreases after a large amount of NH_x is oxidized by either hydrogen radicals or self-bonding, thus resulting in lower NO emissions in rich conditions [12]. In stoichiometric conditions, OH radicals attack ammonia to produce NH_2 and H_2 . It is worth mentioning that HNO has proven to be the most important intermediate in NO formation, accounting for 70% of the intermediates measured in fuel-lean conditions [12].

The extended Zeldovich mechanism (Equations 1.2-1.4) describes the production of thermal NO_x .





Here, the oxidation of dissociated nitrogen molecules at high temperatures (typically above 1800K) results in NO [17]. The first reaction is the rate-limiting step, requiring high temperatures to cleave the N—N covalent bond. The Zeldovich mechanism is applicable in combustion of hydrocarbons only at high temperatures, but is present in ammonia combustion at lower temperatures. However, there is evidence that its net contribution to NO concentration is negligible as Equation (1.2) does not respond significantly to an increase in temperature [5]. DeSoete et al. proposed a global mechanism for the formation of NO based on the oxidation of nitrogen-containing species including NH₃. They concluded that higher oxygen availability produces NO more quickly than the Zeldovich mechanism, thus explaining the formation of NO at temperatures below 1800K [18]. Since adding hydrogen increases flame temperature, it would follow that thermal NO_x production would be greater in NH₃/H₂ mixtures. However, these findings suggest that it could be possible to take advantage of the improved combustion properties in NH₃/H₂ mixtures without increasing NO emissions by a detrimental degree.

A more nuanced examination of NO formation based on the curvatures of NH₃/H₂/N₂/air flames was performed by Netzer et. al. A two-dimensional direct numerical simulation (2-D DNS) based on an updated nitrogen chemistry set from the San Diego mechanisms was performed [19]. Fundamental characteristics of a wrinkled NH₃/H₂/N₂/air flame were investigated to quantify and explain the trends of NO mole fractions within the flame region. A range of equivalence ratios (0.3-1.1) were tested in a gas turbine combustion simulation, comparing two fuel blends: 40% NH₃, 45% H₂, 15% N₂ (blend A) and 72% NH₃, 21% H₂, 7% N₂ (blend B). Their work provides detailed insights into the spatial patterns of NO formation within the flames and enables an improved understanding of the chemical pathways. At lower equivalence ratios (0.3-0.8), large variations in the temporal evolution of the flame fronts led to different flame velocities, and prevented the simulation from producing flames with identical wrinkling. This suggests that stable flames are not attainable at lower equivalence ratios. At higher equivalence ratios, the portion of the flame with low values of heat release rate had the highest NO concentrations. Netzer et. al inferred that the formation patterns of NO are not correlated with the local temperature, suggesting that the Zeldovich mechanism is not the main cause for NO production. They also observed increases and decreases for the local equivalence ratio depending on the global equivalence ratio. These local changes alluded to a differential acceleration of the flame front that resulted in higher degrees of flame wrinkling and larger flame surface areas. Steady state mass fractions were found to correlate well with the local equivalence ratios and corresponding oxygen level. Lean conditions presented two regions: one with increased OH activity in which the maximum NO concentration occurred close to the reaction zone of the flame and the maximum temperature occurred downstream of the flame, in the post-flame zone; another

with reduced OH activity in which NO concentration peaks were found downstream of the reaction zone, in concert with the maximum temperature. Rich conditions, ($\phi > 0.9$) presented only one region where NO concentration peaked shortly after the flame reaction layer, and remained constant further downstream. Variations in the local equivalence ratios converged to the initial global equivalence ratio further downstream. Netzer et. al concluded that fast diffusion of hydrogen into the convex portions of the flame front leads to local increases in the equivalence ratio, which prominently affects NO formation. In globally lean conditions, local increases in ϕ strengthened NO formation. In globally rich conditions, local increases in ϕ weakened NO formation, with the availability of an oxidizer being the limiting factor. Furthermore, they found that blend A with a higher hydrogen content produced more NO (blend B exhibited a peak NO mass fraction 35% lower compared to that of blend A) due to an increase in the OH radical concentration [19]. Importantly, the findings of Netzer et al. and DeSoete et al. are consistent: the Zeldovich mechanism is not the most prominent contributor to NO formation. Reducing NO emissions in ammonia combustion appears to be a greater function of hydrogen-oxygen interactions, which is more a function of equivalence ratio than of temperature. Therefore, the benefits of combusting NH_3/H_2 blends can still be taken advantage of, while strategies to reduce the formation of non-thermal NO_x should be developed.

Hayakawa et al. developed detailed mechanisms to predict NO_x emissions. [20]. They examined the formation of NO and reduction reactions to understand an observed decrease in the NO mole fraction in the post flame region based on the pathway shown in Figure 1.9. The researchers concluded that the reduction rate of NO into N_2 , N_2H and N_2O was much faster than the formation rate of NO from HNO (4.3×10^{-7} vs 2.61×10^{-7} mol/cm², respectively). Furthermore, increasing the operating pressure resulted in a decrease in the total NO mole fraction due to a reduction of the formation of the HNO radical. Numerous studies demonstrated that increasing pressure reduces NO_x production [13]. In fuel rich mixtures, three-body, pressure sensitive reactions are promoted. This is largely attributed to the decrease in OH radical concentration under high pressure, which constrains the $\text{H} + \text{OH} + \text{M} = \text{H}_2\text{O} + \text{M}$ reaction [12]. However, the benefit of increasing pressure (reduced NO_x emissions) exists in competition with a decrease in laminar burning velocity. This trade-off also deserves consideration in determining optimal operating conditions in which to combust ammonia fuel mixtures.

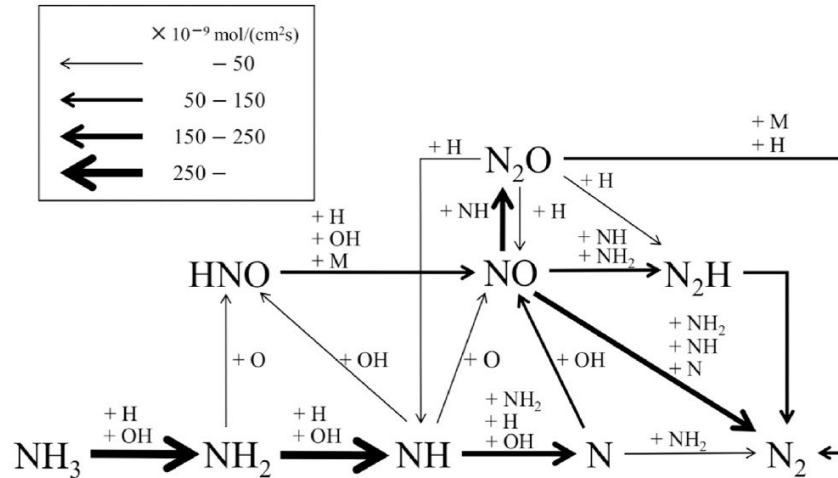


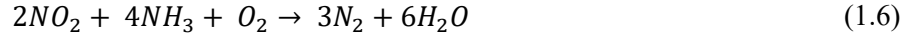
Figure 1.9 Reaction flow diagram of fuel rich ammonia/air flame at 0.1 MPa in the downstream region of the flame. Reprinted from reference [20] with permission from Elsevier.

1.4.3 Ammonia Slip

Another concern regarding ammonia combustion is the possibility of ammonia-slip. Rocha et. al found this phenomenon occurs under fuel rich conditions, with 46 ppm of ammonia slip measured, while only 0.1 ppm was measured for lean conditions [21]. Westlye et. al gathered measurements from a spark ignition engine burning an 80/20% blend of NH_3/H_2 respectively to determine the amount of unburned NH_3 . They determined that the largest source of unburned fuel was due to an accumulation of NH_3 in the combustion chamber crevices. Heat lost at the chamber walls allows NH_3 to dissolve into condensed water vapor produced from combustion. Unburned fuel was not affected by the excess air ratio but varied based on the compression ratio as demonstrated in the figure below. The EURO IV requires NH_3 -slip to be below 25ppm, far below the measured 1000 ppm of this experiment. However, the amount of NH_3 released into the atmosphere could be reduced by using the unburned ammonia to treat NO_x emissions via single catalytic reduction (SCR) or single non-catalytic reduction (SNCR) in the exhaust [17].

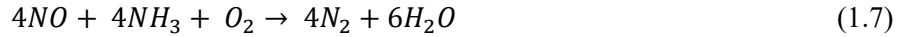
Ammonia has been used as the reagent in single catalytic reduction of NO_x since 1986 and is applied in over 90% of current SCR applications [22]. In SCR, a catalyst at $\sim 300\text{-}400^\circ\text{C}$ promotes a reaction between NO_x and the injection reagent, commonly vaporized NH_3 , to produce N_2 and water vapor (Equations 1.4-1.5).





Ammonia chemisorbs into the catalyst's active sites and reacts with NO_x in the flue, resulting in over 90% reduction in NO_x emissions. Optimum SCR performance occurs when the reagent is well mixed with the flue gas and is proportional to the NO_x that reaches the catalyst [22].

Ammonia is also widely used in single non-catalytic reduction, where nitrogen-containing chemicals selectively react with NO in the presence of oxygen to form N₂ and water vapor (Equation 1.6).



Because SNCR does not involve a catalyst, the reaction requires much higher temperatures, ~850-1050 °C, yet still below the adiabatic flame temperatures of ammonia-based fuels (> 2000 °C). Additionally, 3-4 times the amount of reagent used in SCR is required to achieve a similar NO_x reduction via SNCR. SNCR more commonly results in 20-50% NO_x reduction [22]. In either case, it is possible that a degree of ammonia slip is advantageous – is it reasonable to assume that unburned ammonia would be well mixed with the flue gas, and able to reduce NO_x emissions with or without the presence of a catalyst. Combustion in rich conditions would create an environment to have sufficient NH₃ present in the flue, decreasing NO_x concentrations that are already lower in rich conditions.

1.4.4 Summary of Ammonia Combustion Trade-offs

Based on the literature, a number of trade-offs should be optimized for integrating ammonia as a carbon-free fuel. Adding hydrogen to create NH₃/H₂ mixtures has the benefit of increasing laminar burning velocity at an exponential rate, which increases burning efficiency and power generation. Additional hydrogen also reduces the minimum ignition energy, widening the flammability range of ammonia and making NH₃/H₂ mixtures more readily combustible in already-existing combustion power generation systems. Higher LBVs and lower-point ignition have the combinatorial effect of increasing flame stability, making continuous combustion and power generation a reality. However, additional hydrogen is also associated with higher NO_x emissions, partially due to a greater production of thermal NO_x, but more substantially due to increased interaction between hydrogen and oxygen radicals in the combustion mechanisms.

Similarly, conducting ammonia combustion at elevated pressures has the benefit of reducing NO_x formation, but at the cost of reducing laminar burning velocity. Beneficially, the degree of reduction is relatively low (as seen in Figure 1.4), but still presents operating pressure as a key parameter for optimization.

The trade-off presented in varying equivalence ratio is also of importance. Increasing equivalence ratio effectively decreases NO_x formation, but at the cost of reducing laminar burning velocity in lean and rich

conditions. Only slightly fuel-rich mixtures ($1.0 < \phi < 1.3$) demonstrate the highest laminar burning velocities compared to very lean and very rich mixtures (Figure 1.5).

1.5 Hydrogen-Promoted vs. Cracked Ammonia Fuel Mixtures

A final potential trade-off exists between pure NH_3/H_2 mixtures, and $\text{NH}_3/\text{H}_2/\text{N}_2$ mixtures made from cracked ammonia. This comparison has received less attention but presents an opportunity to further refine ammonia-based combustion for timely applications.

Most studies have focused on NH_3/H_2 blends, which are achieved through directly blending ammonia and hydrogen. However, in practice, H_2 provided by ammonia cracking in a packed bed reactor (PBR) creates a $\text{NH}_3/\text{H}_2/\text{N}_2$ mixture with $\text{H}_2:\text{N}_2$ present in a 3:1 ratio. The additional N_2 is a diluent, which will reduce flame temperature and speed. An advantage of the catalytic membrane reformer (CMR) developed by Sitar et. al is that the nitrogen is rejected, delivering a NH_3/H_2 blend. The effect of extracting N_2 from the fuel on nitrogen oxide formation has not yet been clearly established.

Goldmann et. al developed empirical correlations to predict LBVs based on fuel-hydrogen mole fraction, equivalence ratio, temperature, and pressure [23]. They developed correlations for neat ammonia combustion, NH_3/H_2 combustion, and $\text{NH}_3/\text{H}_2/\text{N}_2$ combustion. Using their regressions we calculated the LBV for both NH_3/H_2 and $\text{NH}_3/\text{H}_2/\text{N}_2$ fuel mixtures across a range of equivalence ratios and fuel-hydrogen mole fractions and demonstrated a lower flame speed in all conditions when N_2 is present (Figure 1.10). For both cases, increasing hydrogen content results in faster LBVs. Goldmann's correlation-based equations demonstrate there is a marked difference between the two fuel mixtures in terms of flame speed, suggesting that nitrogen slows flame propagation. Thus to achieve a desired flame speed, one would require less ammonia cracking with N_2 removal. This is one direct benefit of N_2 removal, but it brings to question whether the presence of N_2 also impacts flame products, especially NO_x . Therefore, this work examines the difference in emissions between NH_3/H_2 and $\text{NH}_3/\text{H}_2/\text{N}_2$ fuel mixtures at equivalence ratio ranging from 0.8-1.1, and fuel-hydrogen mole fraction ranging from 0.15-0.50 to address the following hypothesis: $\text{NH}_3/\text{H}_2/\text{N}_2$ fuel mixtures produce higher NO_x concentrations due to the presence of additional nitrogen.

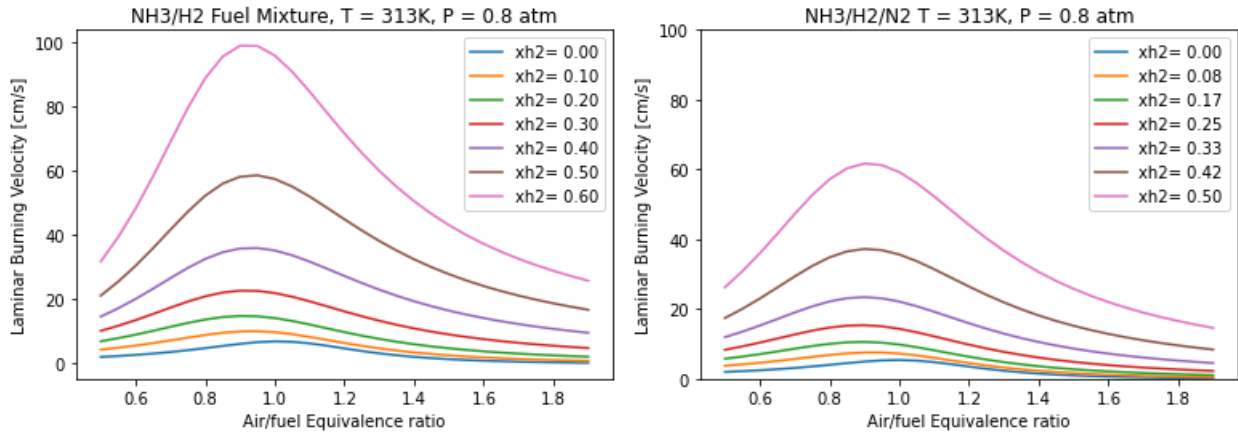


Figure 1.10 Laminar burning velocity profiles of (a) $\text{NH}_3/\text{H}_2/\text{Air}$ flames and (b) $\text{NH}_3/\text{H}_2/\text{N}_2/\text{Air}$ flames across a range of equivalence ratios from 0.5-1.9 and fuel-hydrogen mole fractions from 0.0-0.5.

There have been limited studies directly comparing these two fuel blends (with and without N_2). Meng et. al compared the NO emissions of the two fuel blends with various cracking ratios. These studies were performed in a turbulent burner at extremely fuel lean conditions ($\phi = 0.5$) characteristic of turbine systems. The chemiluminescence of NO was recorded with a high-speed camera paired with an image intensifier. Their results showed that the extraction of nitrogen had negligible effect on the NO_x measured in gas turbines (Figure 1.11).

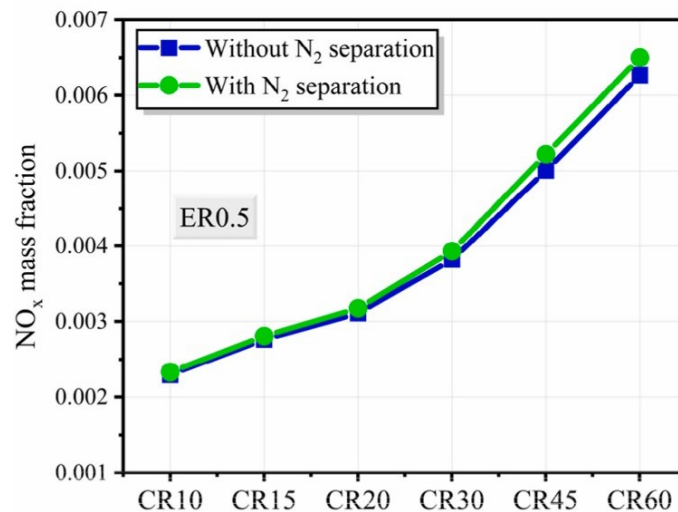


Figure 1.11 Variations of NO_x (NO , NO_2 and N_2O) for various compression ratios. Reprinted from reference [24] with permission from Elsevier.

In contrast, the work of Frigo and co-workers showed significant benefits for N_2 rejection. In two separate studies, they examined the NO_x emissions of a spark ignition engine as a function of revolutions per minute (rpm). In [25] an NH_3/H_2 fuel mixture was used, while a cracking reactor was used in [26] to produce an $NH_3/H_2/N_2$ fuel mixture. Both fuels were tested at an equivalence ratio of 1.0. The NH_3/H_2 fuel mixture produced NO_x in the range of ~ 1550 - 1700 ppm, while the $NH_3/H_2/N_2$ fuel mixture produced more than 3000 ppm at the minimum hydrogen content to power the SI engine (Figure 1.11). A comparison of these studies shows that the extraction of nitrogen produced from cracked ammonia reduces NO_x emissions by nearly half compared to mixtures with N_2 . Additional benefits of extracting N_2 include higher power output and greater operational stability. Thus it appears that the impact of N_2 on NO_x production varies strongly with specific conditions.

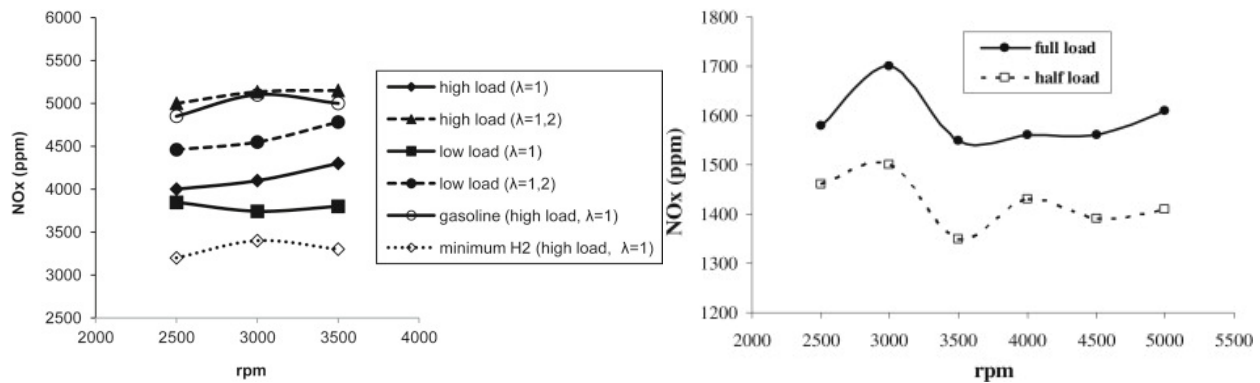


Figure 1.12 (a) Comparison of NO_x emissions with $NH_3/H_2/N_2$ fuel reprinted from Ref. [27] with permission from Elsevier, and (b) NO_x emissions with NH_3/H_2 fuel, $\phi = 1.0$, reprinted from Ref. [25] with permission from Elsevier.

1.6 Goals of this Thesis Work

The purpose of this study was to characterize and compare NO_x emissions in both NH_3/H_2 and $NH_3/H_2/N_2$ fuel mixtures, which was accomplished via five fundamental goals. The first goal was to build a well-defined, one-dimensional burner stabilized flat flame system from which to study the flame characteristic and emissions of the two fuel blends. The second goal of this study was to determine the range of x_{H_2} , ϕ , and volumetric flow rate of the fuel and oxidizer (Q_T) at which flat, stable flames occurred. The third goal was to experimentally characterize NO_x emissions. NO_x emissions across the range of flat-flame operability were measured using a calibrated NO_x analyzer and a calibrated NO_x detector while the fuel/oxidizer volumetric flow rate was held constant. The fourth goal of this study was to validate the experimental results based on Chemkin simulations using the premixed laminar stabilized

burner code and the combustion mechanism developed by Meng et. al [24]. Due to discrepancies between the experimental and model NO_x concentrations, additional experiments were conducted to determine whether selective catalytic reduction (SCR) or selective non-catalytic reduction (SNCR) was occurring inside the sampling tube. The final goal of this study is to propose areas of interest for further research in refining and applying ammonia as an alternative fuel.

CHAPTER 2 MATERIALS AND METHODS

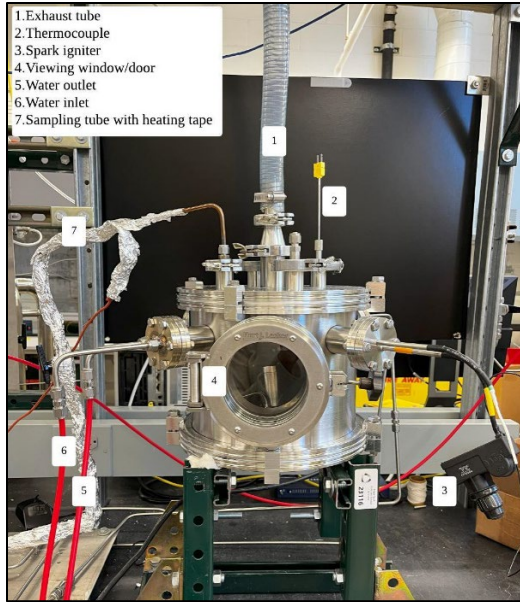
2.1 Materials

The primary goal of this work was to quantify NO_x emissions produced from NH_3/H_2 and $\text{NH}_3/\text{H}_2/\text{N}_2$ fuel mixtures as a function of fuel-hydrogen mole fraction (x_{H_2}) and equivalence ratio (ϕ). This chapter describes how the first goal of this study, to build a well-defined, one-dimensional burner stabilized flat flame system from which to study the flame, was accomplished.

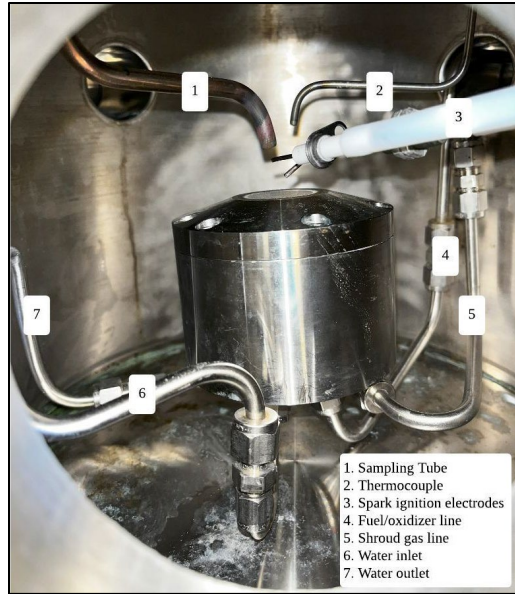
Figure 2.1 shows photographs and a process flow diagram of the apparatus employed in this work. All experiments were conducted in a $9.5 \times 10^{-3} \text{ m}^3$ 316 stainless-steel cylindrical combustion chamber equipped with a $7.8 \times 10^{-3} \text{ m}^2$ inch viewing window/door. The system was mounted under a drop hood and all experiments were conducted at nominally ambient pressure (~ 0.8 bar in Golden, CO). The use of a vacuum chamber and associated fittings (Conflat flanges, O-ring seals, etc.) was used to both prevent atmospheric oxygen from entering the chamber as well as prevent ammonia/hydrogen blends from entering the ambient.

A “McKenna burner” sourced from Holthuis and Associates was installed at the center of the chamber (Figure 2.2). The burner consists of a 316 stainless-steel porous sintered burner plate (2.5cm in diameter), with an Archimedean spiral circuit for water/coolant flow. The cooling circuit reduces radial temperature gradients within the main body of the burner. A coaxial shroud ring surrounds the burner plate, stabilizing the flame and shielding it from the environment of the combustion chamber. A 0.25-inch compression fitting at the bottom of the housing evenly distributes the fuel mixture (the oxidizer and fuel) across the sintered plate. Similarly, the shroud gas is delivered through a 0.25-inch compression fitting in the main body of the burner.

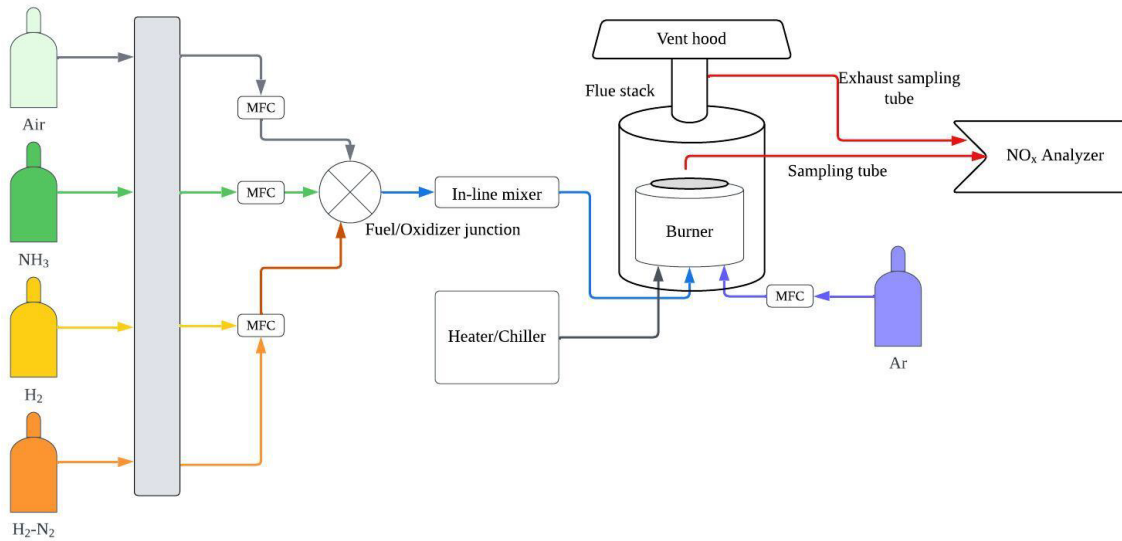
The chamber had four 2-inch conflat flanges (LDS Vacuum) that allowed throughput delivery of fluids to the chamber. Two flanges were modified with 0.25-inch male NPTs to deliver the fuel/oxidizer mixture, shroud gas, and cooling water to the burner. The cooling water was delivered from a recirculating chiller that was used to control the flame inlet temperature. Another flange was dedicated to the ignition source, which was a simple battery-powered, spark ignition switch kit. The electrodes were threaded through a flange with two hollow $1/8^{\text{th}}$ inch prongs and suspended 0.75 inches above the center of the burner to ignite the fuel. The ignition wires were sealed with shrink wrap to insulate the hollow prongs. The fourth flange was fitted with a digital pressure gauge on the chamber. The top of the chamber had four 1-inch conflat adapters, two of which remained sealed with silicone rubber seals (LDS Vacuum). One was fitted with an NPT for the sampling tube, and one was fitted with an NPT to measure the temperature of the flame with a type-K thermocouple.



(a) Vacuum chamber exterior



(b) Vacuum chamber interior



(c) Process flow diagram

Figure 2.1 (a) Photograph of the vacuum chamber, (b) photograph of the inside of the chamber, and (c) process flow diagram of the apparatus employed in this work.

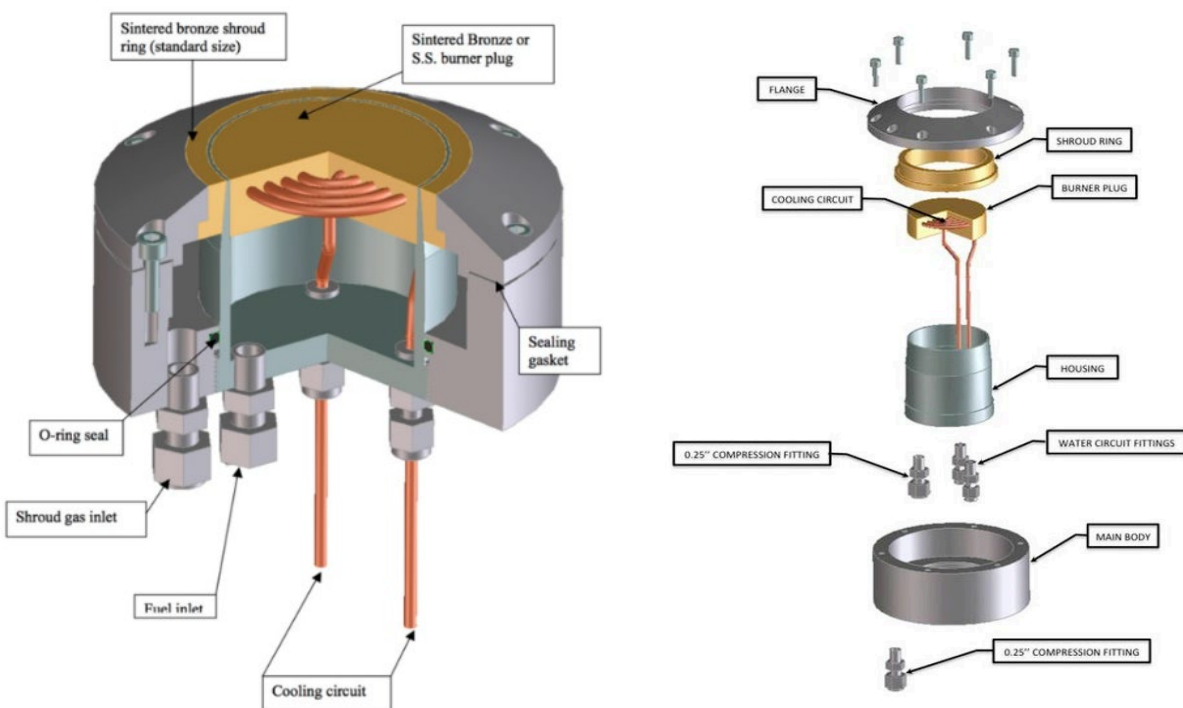


Figure 2.2 (a) Photograph and (b) schematic diagrams of burner interior. Reprinted from [28] with permission from Leneke Holthuis.

All gases used in this study were ultrahigh-purity (UHP) grade sourced from General Air and delivered to the chamber using calibrated Alborg electronic mass flow controllers (MFC). The $\text{NH}_3/\text{H}_2/\text{air}$ blends were made using anhydrous ammonia, hydrogen, and grade ultra zero air. The $\text{NH}_3/\text{H}_2/\text{N}_2/\text{air}$ blends were made the same way, except the hydrogen was replaced with a cylinder composed of 75% hydrogen and 25% nitrogen to simulate 100% cracked ammonia. Each gas flowed from its cylinder to the gas delivery panel, which connected to its MFC. A junction connected the fuel components and oxidizer, which then passed through an in-line mixer. The fuel-oxidizer mix was fed to the 0.25-inch compression fitting on the burner, where it encountered the water flow of the burner which controlled the temperature of the mixture. The shroud gas (UHP argon) was fed through its own distinct line and MFC, directly to the shroud inlet.

The combustion products were sampled through a 0.25-inch outer-diameter (OD) stainless steel tube whose sampling position could be adjusted between 0.25 - 5.0 cm above the center of the burner. The tube interior had an inert coating (Siltek Sulfinert) that makes it nominally unreactive with water vapor, ammonia, and nitrogen oxides. The driving force for sampling was provided by a vacuum pump in the NO_x analyzer (described in the next paragraph) that created a pressure gradient of approximately 15-40 mbar in the reaction chamber. The approximate sample flow rate was 600 sccm, which was 26.06-27.31%

of the total flow. To avoid condensation between the sampling point and the inlet to the NO_x analyzer, the sampling line was heated to 190° C using a Bristek heating tape.

Nitrogen oxide measurements were collected using a calibrated ECO Physics nCLD 822n analyzer (Figure 2.3). The analyzer employs chemiluminescence to measure nitrogen oxides, which allows for the detection of extremely low concentrations of NO. The chemiluminescence signal is detected photoelectrically, with the radiation emission wavelength ranging from 600 – 3000 nm, and an intensity maximum of 1200 nm. The nCLD 822n analyzer is a two-channel instrument for simultaneous measurements of NO and NO_x. Each channel is equipped with a photo multiplier (PMT) and reaction chamber, which is where the chemiluminescence reactions take place. The photomultiplier housing is flushed with a flow of dry air to prevent condensation in the PMT tubes.

In the reaction scheme via chemiluminescence, NO reacts with ozone produced in the ozone generator from dried ambient air. NO concentrations are interpreted based on their proportionality to the photoelectric chemiluminescence signal. NO₂ measurements are based on reducing NO₂ to NO, then using chemiluminescence to determine the amount of NO₂ that was converted to NO (equations 2.1-2.4). A catalyst that converts amines to NO, and a converter that converts only NO₂ to NO are used to distinguish the specific NO_x concentrations. Any unreacted ozone is destroyed in the ozone scrubber located on the vacuum pump.



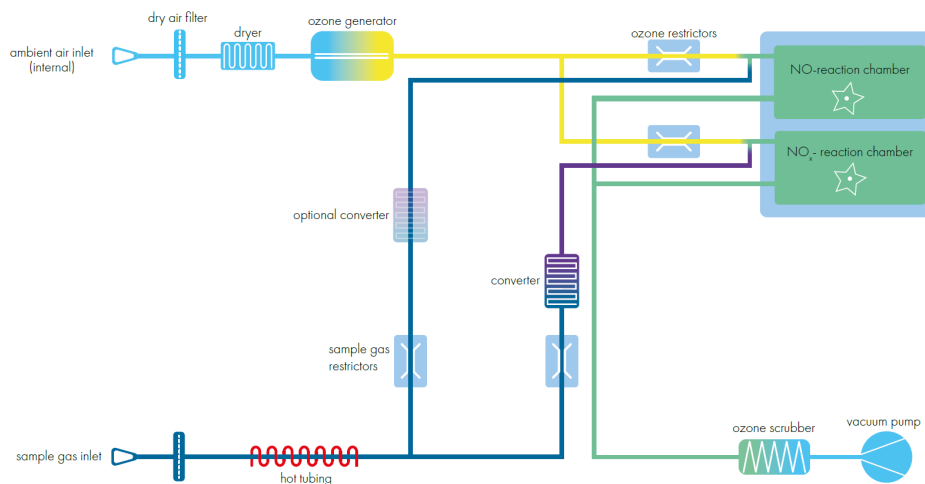
Quenching is the phenomenon in which the presence of interfering components, such as colliding molecules (M in equation 2.4), reduces the NO chemiluminescence signal. Water quenches the NO signal more effectively than N₂ or O₂, hence why heating the sampling tube to at least 180 °C is important. A second type of interference occurs in the NO₂-NO converter when nitrogen compounds are converted to NO, such as nitric acid (HNO₃) and ammonia, and produce erroneously high NO₂ measurements.

The analyzer is capable of measuring concentrations from 5-5000 ppm, with an uncertainty of 1% the desired range (5000, 500, 50 and 10 ppm). The sensitivity of the instrument declines when measuring

humid samples. The analyzer displays the measurements as three components: NO_x , NO and NO_2 . NO is measured through chemiluminescence, as described above, and NO_2 is measured through converting it to NO . The NO_x measurement is a sum of NO and NO_2 . In some instances, the analyzer reported concentrations of NO_2 less than zero due to this summation method. Therefore, this study uses the NO measurements as the fundamental metric of observation.



(a) Front side of NO_x analyzer and graphic user interface.



(b) Analyzer process flow diagram for collecting and interpreting NO_x measurements.

Figure 2.3 (a) NO_x analyzer, (b) Analyzer process flow diagram. Images from ECO Physics user manual [29]. Reprinted with permission from ECO Physics.

The NO_x analyzer presents the measurements via a graphical user interface (GUI). NO and NO_2 measurements are collected every millisecond in parts-per-million (ppm). The GUI presents a real-time graphical relationship between time on the x-axis, and NO_x , NO and NO_2 concentrations on the y-axis. There was negligible lag-time between what was occurring in the vacuum chamber, and what was displayed on the analyzer interface. For example, if the flame extinguished, the NO_x , NO and NO_2

concentrations immediately read 0-1.4ppm, which was the value when atmospheric air passed through the analyzer.

The NO_x analyzer was calibrated using a calibration gas composed of 4000 ppm of NO in nitrogen. A plastic 0.25 inch outer-diameter tube was used to connect the gas to the analyzer. A T-shaped junction was placed between the calibration gas and the analyzer to prevent over-pressuring the analyzer. A direct calibration with a maximum concentration of 4040 ppm of NO was performed with 0.931% error.

2.2 Experimental Design

For fundamental studies and to facilitate comparison with models, it was important to first define the operating conditions in which flat, stable flames were observed. Figure 2.4 displays photographs of H_2/NH_3 flames provided by the National Energy Technology Laboratory (NETL). From left to right the hydrogen concentration is decreasing. The first three images are well-defined flat flames. Although difficult to see, there are ripples developing in the 4th flame, and chaotic wrinkles in the fifth. The flame is beginning to lift off the burner in the last photo.



Figure 2.4 Photographs of H_2/NH_3 flat flames ranging from 70% H_2 on the left to 20% on the right in 10% increments. The ideal flat flame condition is lost in the last 2-3 images. Reprinted from Ref. [30], an open source presentation.

Therefore, the goal of the first set of experiments was to define the range of conditions in which ignitable, 1-dimensional, flat, stable flames were achieved. The “conditions” include varying equivalence ratio $0.8 < \phi < 1.1$, varying fuel-hydrogen composition (x_{H_2}) from 10-50%, and varying total volumetric flow rate, Q_T , which refers to the sum of the fuel and oxidizer volumetric flow rates. Goldmann’s correlation equations were used to calculate predicted LBV values at 40 °C (unburned gas temperature) and 0.8 atm (ambient pressure), across a range of fuel compositions (x_{H_2} , x_{N_2}), and equivalence ratios (as described in Chapter 1.5). Then, the predicted LBV values were used to calculate theoretical volumetric flow rate (Q_T) values normalized to the area of the burner. An example of the process and equations are described in Table 2.1.

Table 2.1 Calculations and methodology for experimental flow rates

Step	Variable/Equation	Rationale
1	$U_{desired} = 9.8 \text{ cm/s}$	Estimate of laminar flame speed at burner surface from correlations
2	$Q_{desired} = U_{desired} * A$	Calculate the desired volumetric flow rate based on desired LBV and area of the burner. This is used to create a proportionality among the flow rates.
3	$Q_{STD} = Q_{desired} * P_{atm} * \frac{T_{STD}}{T_{fuel}}$	Convert volumetric flow rate at experimental conditions to standard conditions.
4	$Q_T = S_L * Q_{STD} * x_{correlation}$	Calculate total volumetric flow rate based on wanting to achieve a percentage of the predicted LBV from Glaborg correlations
5	$2 \text{ NH}_3 + \text{O}_2 \rightarrow \text{H}_2\text{O} + \text{N}_2$ $2 \text{ H}_2 + \text{O}_2 \rightarrow 2 \text{ H}_2\text{O}$ $O_{2,stoich} = 0.5Q_{H_2} + 0.75Q_{NH_3}$	Calculate the oxygen required for complete combustion in stoichiometric conditions
6	$O_{2,air} = \frac{O_{2,stoich}}{\phi}$	Calculate oxygen required for combustion at the desired equivalence ratio
7	$N_{2,air} = 3.76 O_{2,air}$	Calculate the nitrogen present as a reactant
8	$Q_{T,t} = \sum Q_i$	Total theoretical flow is the sum the preliminary flow rates of all reactants
9	$y_i = \frac{Q_i}{Q_{T,t}}$	Determine the actual mole fraction of each component based on the total theoretical flow and component flow
10	$Q_{i,actual} = y_i * Q_T$	Determine the actual flow of each component to achieve the LBV based on the correlation
11	$x_f = \frac{Q_{T,actual} - 0.5}{0.5}$	Fuel flow correction factor based on maintaining 0.5 SLM of fuel used in each experiment

In order to determine where blow-off occurs (when Q_T was too fast for ignition to occur or presented flame instabilities), volumetric flow rates 10-100% of the predicted value were tested (step 4 in Table 2-1). Another correction factor had to be incorporated to ensure the total fuel supplied to the burner was

constant throughout experiments (step 11 in Table 2.1). The average of the Q_T values in which a flat, stable flame was achieved was used for subsequent experiments. It was important to maintain a constant Q_T value so that the NO_x measurements were not a function of volumetric flow rate while the equivalence ratio and hydrogen composition were varied. The volumetric flow rates to achieve a constant Q_T , and tested in subsequent experiments, are included in Table A.1, Appendix A. Figure 2.5 compares the experimental inlet speed for the fuel/oxidizer mixture to the calculated laminar flame speed based on Goldman's correlation equations. Note that the inlet speed does not indicate the speed of the fully developed flame (LFS). Rather, the comparison provides a prediction for how much the speed of the flame will increase at the end of the flame front as x_{H_2} and equivalence ratio vary.

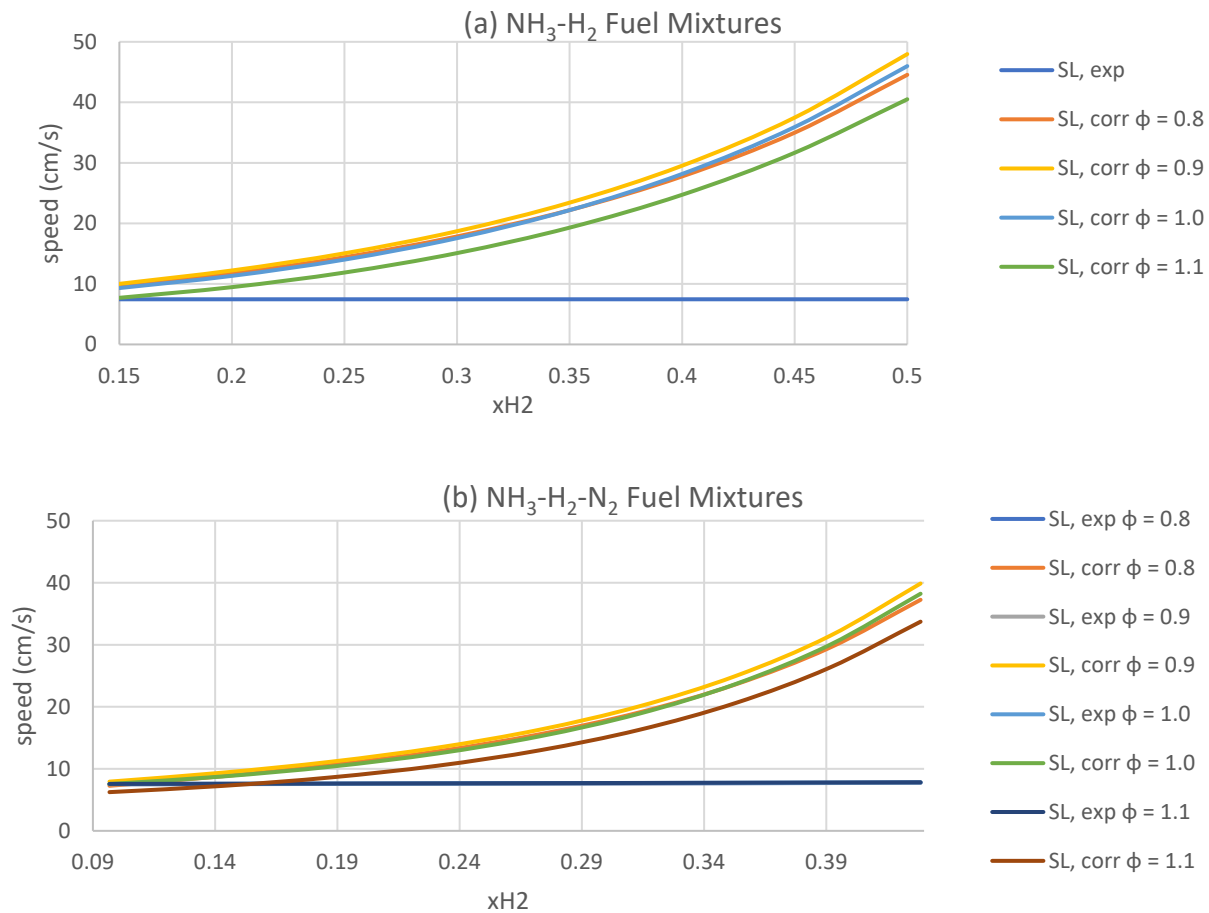


Figure 2.5 Experimental inlet fuel/oxidizer velocity (cm/s) and calculated laminar flame speed for fully developed flames for $0.x_{H_2}$ ranging from 15-50% and 9.67-42.9% for (a) NH_3/H_2 and (b) $NH_3/H_2/N_2$ fuel mixtures respectively.

The shroud gas flow rate varied to have a volumetric flow rate equivalent to that of the fuel/oxidizer mixture delivered to the burner. The flow rate of the shroud gas was determined based on a proportional relationship between the burner area and the shroud gas area.

After defining the range of operating conditions that supported ignitable, 1-D, stable flames, the next goal was to determine the most appropriate height to place the sampling tube above the center of the burner. The first method to accomplish this was by measuring the temperature of the flame at various locations. The rationale was that the height at which the maximum temperature was observed would indicate the location of reaction completion for exothermic reactions, such as combustion. Therefore, taking samples above, but close to the height of maximum temperature would present measurements most representative of the NO_x produced. However, the type-K thermocouples were not compatible with the high temperatures of the flames (maximum reading of ~868 °C), and the radiative heat loss of the flames introduced a large degree of uncertainty into this method. The second method to determine the optimal sampling tube height was to measure NO_x concentrations of each operating condition and four different sampling-tube heights (0.25 cm, 0.50 cm, 1.0 cm, and 2.0 cm above the burner surface). The maximum concentration measured among the four heights was used as the representative NO_x measurement for that condition. This method also accommodated for variations in the flame speed, which varied depending on hydrogen content, thus varying the height at which combustion was complete.

The next set of experiments was measuring the emitted NO_x concentrations. The two fuel blends were compared at the range of operating conditions for stable, flat flames. The NH₃/H₂/air mixtures were made based on the calculations described in Table 2.1. The NH₃/H₂/N₂/air mixtures used the same methodology, however the H₂/N₂ flow rate was determined by the relationship in equation (2.1) to deliver the same hydrogen content to the system.

$$Q_{H_2, N_2} = \frac{Q_{H_2}}{0.75} \quad (2.1)$$

Each experiment began with purging the combustion chamber of atmospheric air by flowing argon into the tank for a minimum of 8 minutes. During the purge, the water heater was turned on to 40 °C – this temperature was chosen to minimize accumulation of condensation in the chamber. MFCs were set to the calculated flow rates. After the flame was ignited, data collection with the NO_x analyzer began. NO_x measurements that gradually decreased over time indicated that atmospheric oxygen was still present in the tank. A steady state was evident once NO_x measurements held a fairly constant value for at least 60 seconds. Samples for each operating condition were collected over a 3-minute time span, with measurements recorded every milli-second. There was confidence that NO_x was not accumulating in the

sampling tube due to the immediate return to pre-flame values when combustion ceased, and results were not skewed.

Samples were collected from the exhaust line of the combustion apparatus (Figure 2.6) at $\phi = 1.0$, and compared with measurements from samples taken directly above the flame. The purpose was to determine whether the shroud gas was diluting the samples taken directly above the flame. The dilution equation (2.2) was used to determine the “actual” NO_x concentration for all samples taken.

$$[\text{NO}_{x,actual}] = [\text{NO}_{x,measured}] * \frac{Q_{T,with Ar}}{Q_{T,without Ar}} \quad (2.2)$$

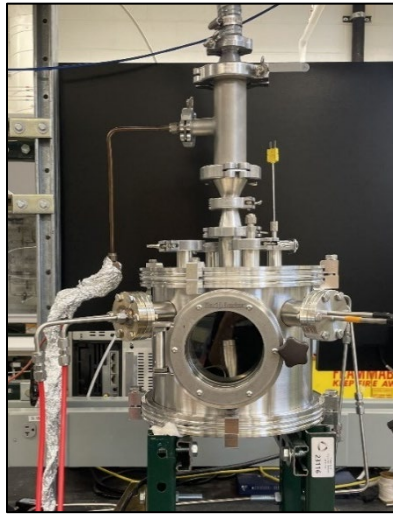


Figure 2.6 Configuration for sampling the exhaust gas.

2.3 Theoretical Modeling

Theoretical NO_x concentrations for flames with $\phi=1.0$ were modeled in Chemkin Ansys software using the mechanism developed by Meng et. al [24]. This model was selected based on its good agreement for predicting NO_x measurements for combustion of NH_3 enriched with oxygen. The thermodynamic, transport, and mechanism data specified by Meng et al. were used and are included in Appendix B. The theoretical modeling provided a basis for comparison for the results from this study for flame profiles, flame velocity, and major and minor species concentrations.

The equilibrium code from Chemkin was used to determine the adiabatic flame temperatures of both fuel mixtures at equivalence ratio 1.0. The “Constant Pressure Enthalpy” problem type was performed to

calculate the maximum flame temperature with a given species composition. The initial temperature of all fuel mixtures (mixture A and B, with x_{H_2} ranging from 0.15-0.50) was set to 313 K (due to the water heater temperature being set to 40 °C), a constant pressure of 0.8 atm, and an estimated equilibrium temperature of 2000 K. The resultant equilibrium temperature (Table B.2, Appendix B) was used to initialize the premixed laminar burner-stabilized flame (PREMIX) code based on a fixed temperature profile.

The PREMIX simulations (schematic in Figure 2.7) consisted of a nonreactive gas mixer at 313 K and 0.8 atm. The inlet volumetric flow rate in standard-cm³/min (scmm), fuel mixture components (excluding air), and component mole fractions for the mixer were specified (Table B.1, Appendix B). The volumetric flow rates were based on the experimental Q_T values, normalized to a 1-cm diameter burner. The equivalence ratio was set to 1.0, and Chemkin determined the required mole fractions for the air-fuel mixture to achieve the desired equivalence ratio. The oxidizer mixture was auto-populated for air. The mixer fed into the burner-stabilized flame module.



Figure 2.7 PREMIX simulation schematic in Chemin with an inlet source, non-reactive mixer, premixed laminar burner-stabilized flame, and outlet flow models (from left to right).

First, the “Fix Gas Temperature” problem type with thermal diffusion, mixture-averaged transport and correction velocity formalism was performed to initialize the PREMIX solution. The temperature profile was initialized by entering an initial guess for the height and temperature range at which the flame reached the adiabatic flame temperature. Table B.2, Appendix B shows the start and end distances (from the burner surface) and start and end temperature values entered for both fuel mixtures as $\phi=1.0$. The end distance is the lowest value that produced a solution, i.e. the closest distance above the burner at which the adiabatic flame temperature could be reached. This initial solution forced the flame to reach the end temperature, and provided composition data for reactants, intermediates, and products. Then, the “Solve Gas Energy Equation” problem type with thermal diffusion, mixture-averaged transport, correction velocity formalism, and an automatic estimated temperature profile was performed.

Table B.3, Appendix B details the solving parameters specified for running the PREMIX code. The values were selected after running the code with variations in all parameters to investigate the degree to which they changed the temperature, NO and NH₃ mole fractions at 15 mm above the burner surface.

Statistical analysis on the temperature, NO and NH₃ mole fraction values informed the uncertainty associated with the PREMIX code. The default solver parameters were used with an absolute tolerance of 1.0×10^{-9} , a relative tolerance of 1.0×10^{-4} . The default output control values for the threshold for species sensitivity, solution data block size, and print level control were also employed. The transport linking data was saved to incorporate the initialized solution from the “Fix Temperature Profile” simulation.

Figure 2.8 compares the experimental fuel/oxidizer velocity fed to the burner and the predicted fuel/oxidizer velocity at the surface of the burner upon ignition, calculated in Chemkin. The LBVs predicted by Chemkin are 25-31% higher than the fed velocity for both mixtures. It is reasonable to assume that upon ignition, the flow rate of the fuel/oxidizer mixture increases to the velocity predicted by Chemkin. This comparison provides confidence that the Chemkin simulations realistically describe the experimental conditions.

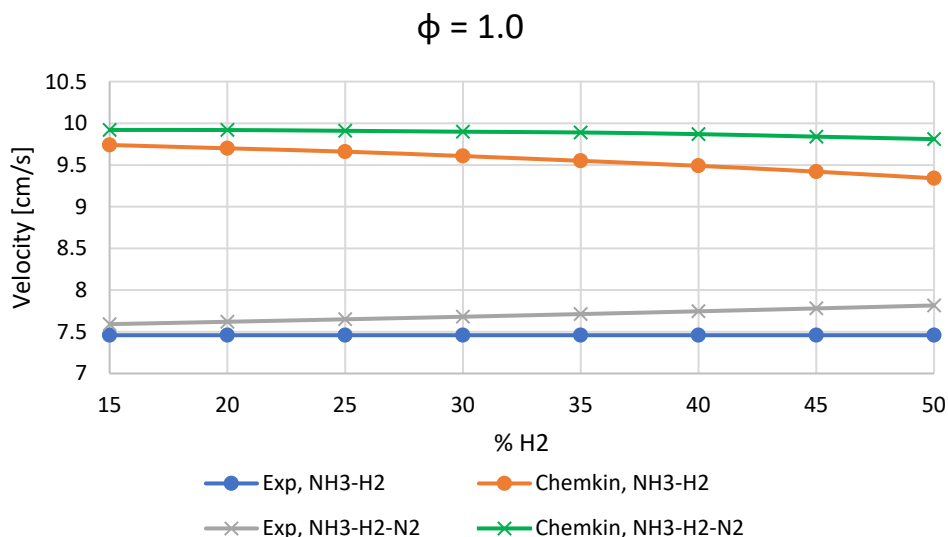


Figure 2.8 Fuel/oxidizer velocity fed to the burner (experimental, Exp) compared to the LBV at the burner surface upon ignition (Chemkin) for NH₃/H₂ and NH₃/H₂/N₂ mixtures at $\phi = 1.0$.

Figure 2.9 (a) displays a typical flame profile, produced using the Chemkin PREMIX code. Specifically this is for a 30% H₂ blend at an equivalence ratio of 1.0. The unburned fuel temperature was 40 °C, and pressure was set to 0.8 atm. Fig. 2.9 (a) plots the major species and temperature while (b) plots the concentration of NO_x emissions and radicals with significant concentrations. The major species include the feed (H₂, NH₃, O₂, N₂) and the product H₂O. The minor species include NO, N₂O, NO₂, which comprise NO_x when summed together as well as other important radicals such as OH and H. The

profiles demonstrate that the combustion reaction occurs within the first 2 mm above the burner surface, with nominal change in temperature and mole fractions in the post-reaction zone. Of the reagents O_2 and NH_3 are completely consumed (< 1 ppm) while a significant amount of H_2 (>6000 ppm) remains in the post combustion region. The product mole fractions H_2O and N_2 increase as expected, and the very high moisture content (30%) is noted. Among the contributors to NO_x , NO_2 peaks at ~ 10 ppm near flame ignition and rapidly declines to negligible levels. Nitrous oxide (N_2O) levels exceed 1000 ppm at the flame front but then exponentially decline to negligible levels. NO builds steadily and saturates at 5000 ppm and remains unchanged. Thus our measurements of “ NO_x ” essentially mean NO and these terms are used interchangeably going forward. Also these predictions suggest measurements of NO_x should not be sensitive to position as long as they are sufficiently downstream (> 3 mm) of the burner. Among the various radicals, most are negligible, yet as shown both H and OH persist at significant quantities (~ 1000 ppm) in the post flame environment. These species, along with H_2 are on the same order of the expected NO and may be important contributors to the differences between model and experiment discussed below.

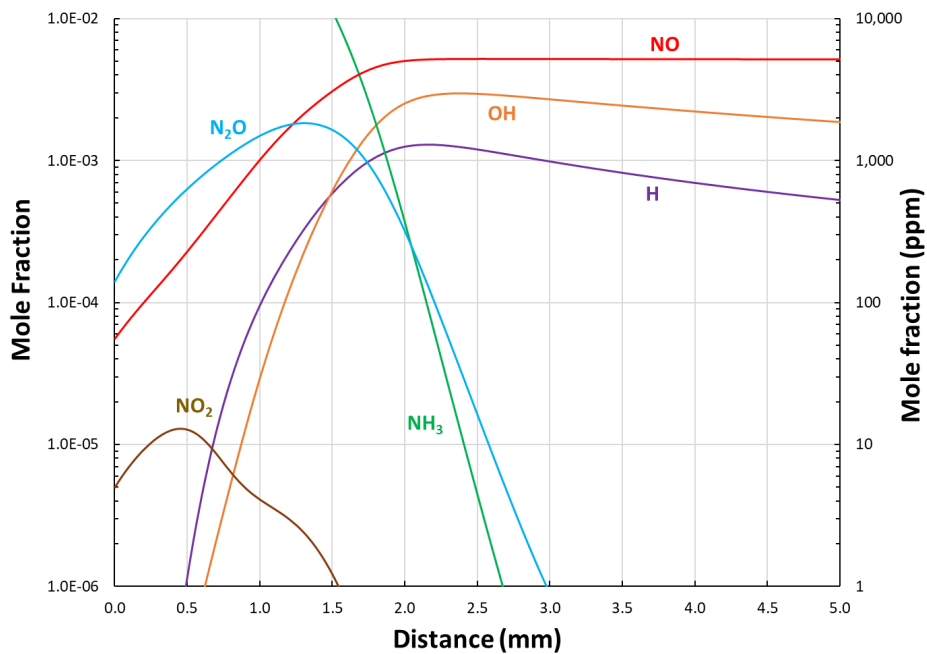
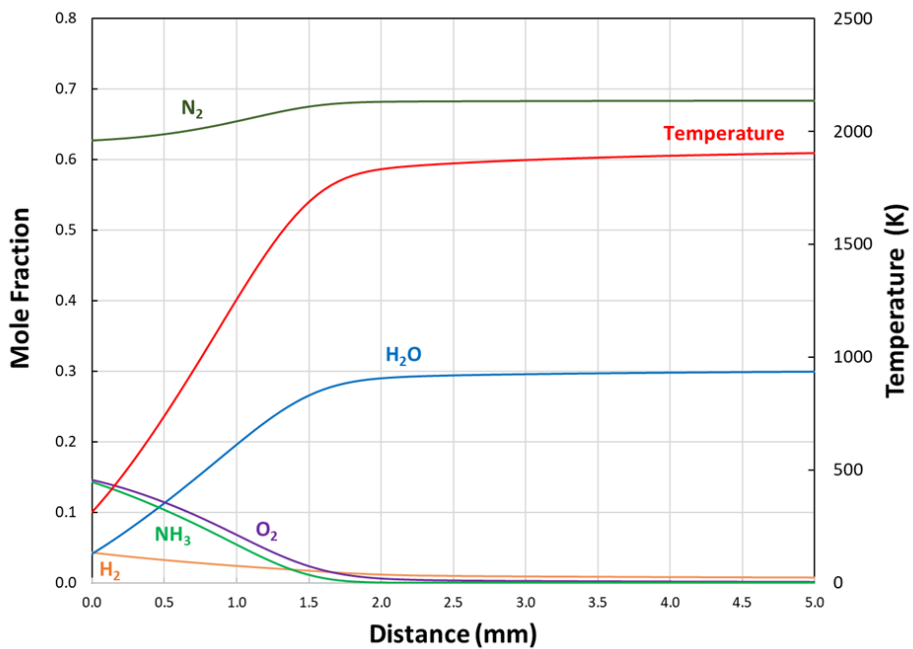


Figure 2.9 Flame profile for 30% H₂, NH₃/H₂ fuel mixture at $\phi = 1.0$ with (a) major species (NH₃, H₂, O₂, H₂O) and temperature and (b) the major impurities including critical NO_x emissions, NH₃ slip, and persistent radicals H and OH.

3.1 Flat Flame Operating Conditions

The second goal of this study was to determine the range of x_{H_2} , ϕ , and fuel/oxidizer volumetric flow rate (Q_T) at which stable, one-dimensional flames occurred. Flame stability is related to the burner structure, equivalence ratio, ignitability, and velocity of the fuel/oxidizer mixture [31]. Flat flames were observed for equivalence ratios ranging from 0.8-1.2, and x_{H_2} ranging from 0.25-1.0. This work focuses on flames with $0.8 \leq \phi \leq 1.1$ and $0.15 \leq x_{H_2} \leq 0.50$. This range for x_{H_2} was selected based on the fuel-hydrogen mole fraction that would most likely be used in pursuing ammonia as an alternative fuel source. Ideally values of $x_{H_2} < 0.15$ would have been studied, however fuels with less than 15% hydrogen did not ignite, and extinguished almost immediately upon decreasing hydrogen to a lower mole fraction. Mixtures with $x_{H_2} > 0.50$ were not considered to limit the scope of this work to majority-ammonia fuels.

As described in Table 2.1, LBVs ranging from 10-100% of the predicted LBV were tested to determine the total volumetric flow rate that resulted in stable, 1-D flames. Q_T (the total volumetric flow rate for the fuel and oxidizer components) varied from 1.170 - 3.544 SLM for the NH_3 - H_2 mixtures, and 1.219 - 3.665 SLM for the NH_3 / H_2 / N_2 mixtures. Q_T values near the lower bound produced unstable flames with a teardrop shape. Q_T values near the upper bound produced stable flames, but with deformities such as small hills throughout the burner surface when $x_{H_2} \geq 0.40$ at all equivalence ratios, and large orange peaks when $x_{H_2} < 0.40$ which indicated the presence of unburned ammonia. The average Q_T at which flat, ignitable flames were observed was determined to be 2.197 SLM. This value was used in subsequent experiments to characterize NO_x emissions as a function of x_{H_2} and equivalence ratio.

Figures 3.1 and 3.2 compare the flame structures of the conditions in which NO_x measurements were studied ($Q_T = 2.197$ SLM, $0.8 \leq \phi \leq 1.1$, and $0.15 \leq x_{H_2} \leq 0.50$). Photos were taken when the sampling tube was 2 cm above the burner surface, which turned red-hot from being so close to a flame for more than 2 minutes. Of note, the flames with less than or equal to 20% hydrogen in the fuel are not considered flat. The consequences of a multi-dimensional flame were high oscillation frequency in the flame diameter, severe curvature at the edges, and spontaneous quenching. These consequences would pose problems if implemented in combustion-based power generation systems. Regardless, this work studied the NO_x emissions for mixtures with less than 20% hydrogen to develop a more broad characterization. The flame operating conditions in which the flame is considered 1-D and stable are marked with a green border around the photo.

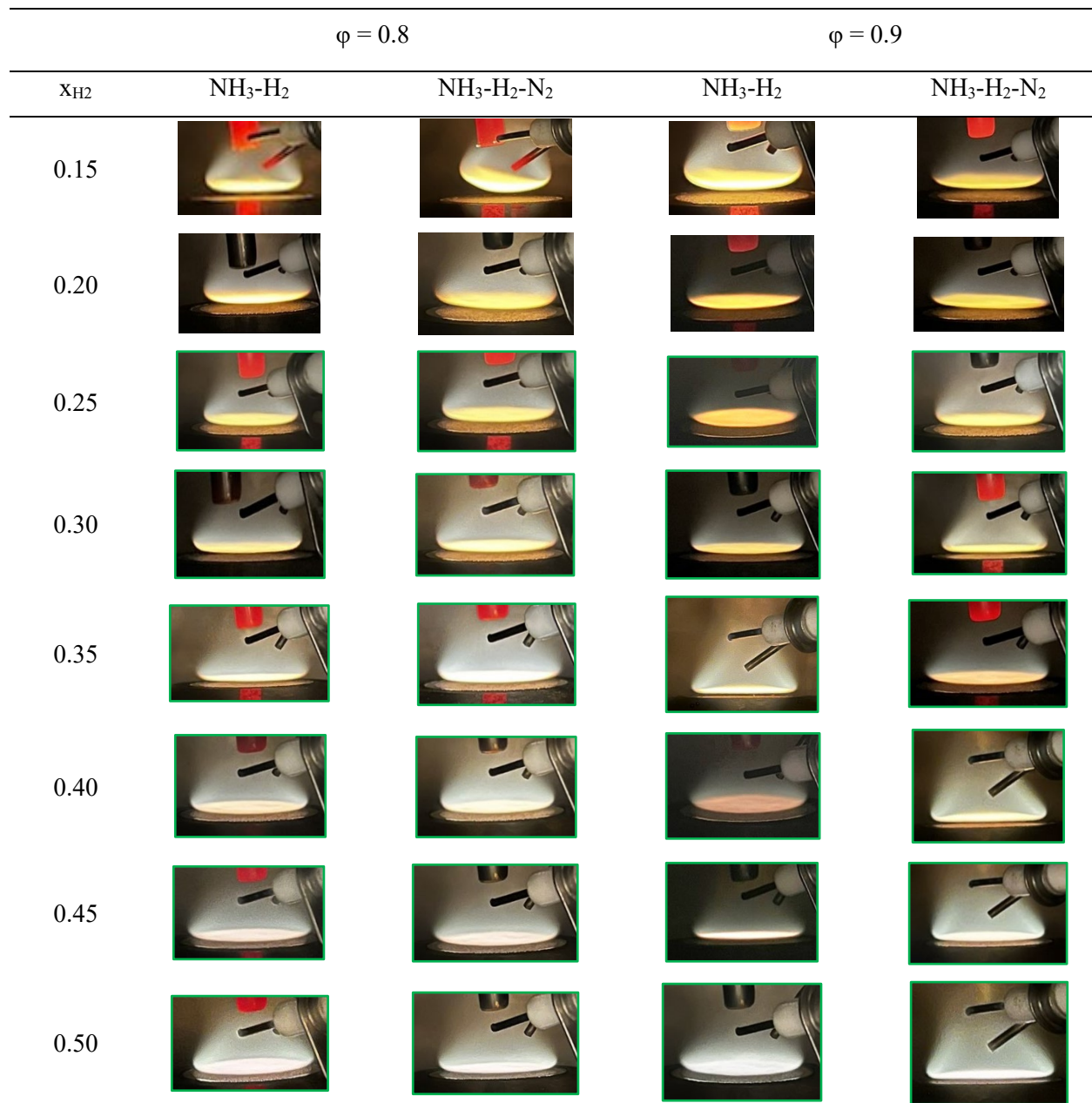


Figure 3.1 Flame profiles for $\phi = 0.8$ and 0.9 .

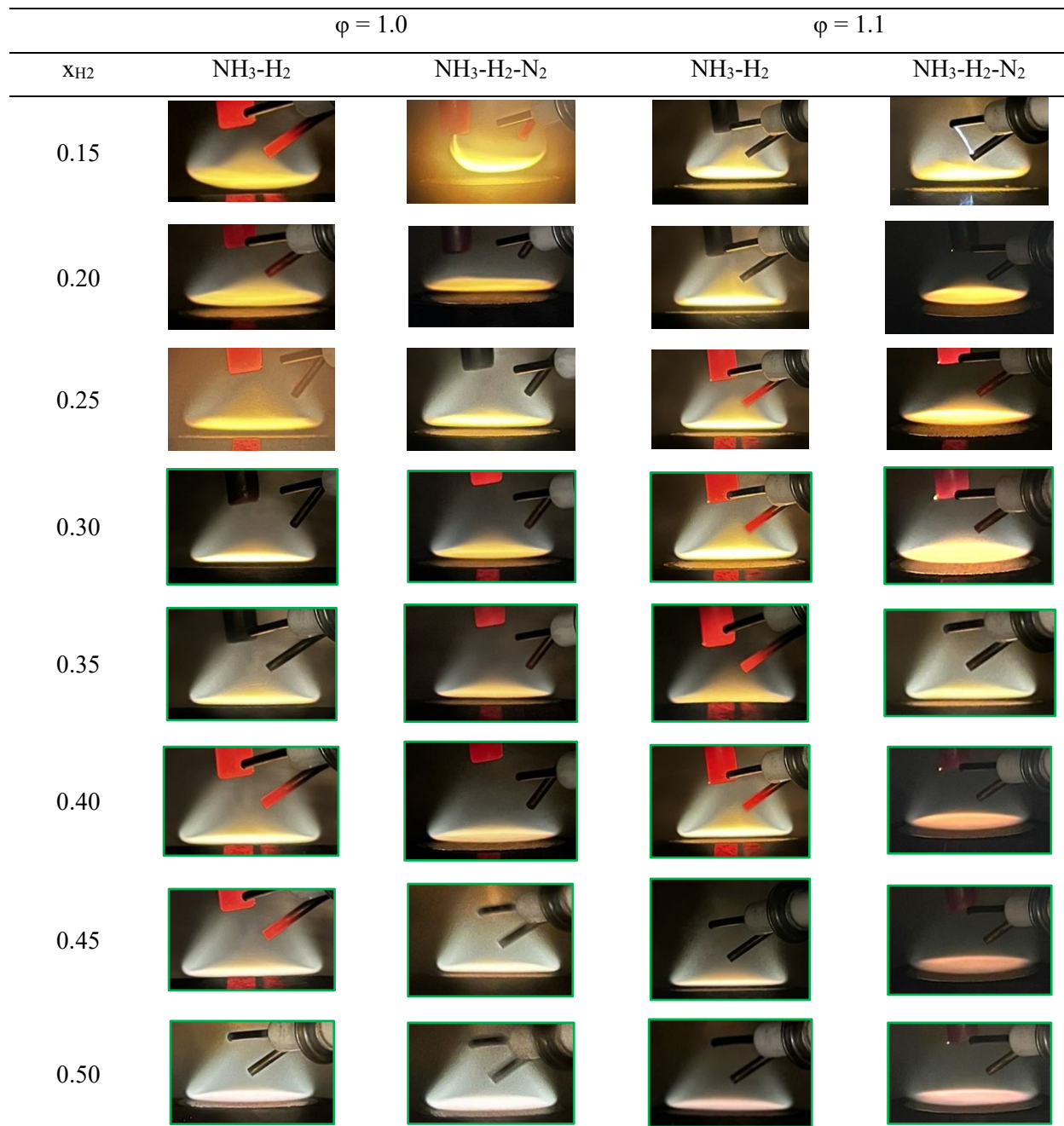


Figure 3.2 Flame profiles for $\phi = 1.0$ and 1.1 .

There was little observable distinction between the flame structures of the two fuel mixtures. The rejection of N₂ extends the stability of NH₃/H₂ mixtures to lower hydrogen fractions at $x_{H_2} = 0.15$ and 0.20 , while for $x_{H_2} \geq 0.25$, the mixtures are nearly indistinguishable to the naked eye. This is likely because quantitatively, the hydrogen supplied to the burner was the same for both fuel mixtures, i.e. the volumetric flow rate for H₂ in the NH₃/H₂ mixture was equal to that of the NH₃/H₂/N₂ mixture. The

structural differences between the mixtures were more observable at lower x_{H_2} values, from 0.15-0.20, likely due to insufficient hydrogen present to overcome the combustion impediments inherent of nitrogen. In all cases, increasing the hydrogen content produced flatter, more stable flames, which is consistent with its combustion promoting effects.

Ignition was an important aspect to observe qualitatively as it is a good indicator of real-world applicability. Ammonia is combustible at concentrations of ~15-28% by volume in air [2]. It was expected that the incorporation of hydrogen would shift the flammability range to a lower range, meaning that less ammonia would be required to ignite a flame. The flammability limits of the two fuel mixtures based on the results of this work are listed in Table 3.1. Note that the lower limit is imposed due to the maximum x_{H_2} value tested in this work being 0.5. As expected, lower proportions of ammonia were required for ignition with the incorporation of hydrogen for both fuel mixtures. The flammability ranges for $NH_3/H_2/N_2$ mixtures was slightly more narrow compared to NH_3/H_2 mixtures due to nitrogen dilution.

Table 3.1 Flammability ranges of NH_3/H_2 and $NH_3/H_2/N_2$ mixtures at various equivalence ratios

ϕ	Flammability range (ammonia % by volume in air)	
	NH_3/H_2	$NH_3/H_2/N_2$
0.8	14.78 – 19.63%	14.24 – 19.30%
0.9	15.17 – 20.99%	14.61 – 19.79%
1.0	15.50 – 21.44%	14.89 – 21.09%
1.1	15.78 – 21.81%	15.18 – 20.55%

Ignition was instant for mixtures with 25-50% hydrogen at all equivalence ratios studied. For $x_{H_2} < 0.25$, the high minimum ignition energy of ammonia dominated, and ignition required multiple sparks from the igniter. Slower ignition times were especially observed in fuel-lean conditions ($\phi < 1.0$) which was likely due to the lower density of hydrogen in the fuel/oxidant mixture. Fuel mixtures with $\leq 20\%$ hydrogen were very difficult to ignite, and often required ignition while providing higher flow rates of hydrogen to the burner, then reducing the flow rate to the desired value. Mixtures with 15% hydrogen did not ignite, and flames were only obtained using the same scaling-back method just described. There was also a marked difference in the ignition speed between NH_3/H_2 and $NH_3/H_2/N_2$ mixtures. NH_3/H_2 mixtures were consistently easier to ignite, while $NH_3/H_2/N_2$ mixtures required multiple sparks even at

x_{H_2} values of 25-40% hydrogen. This can be attributed to the presence of extra nitrogen, which acted as a diluent and combustion inhibitor.

Another qualitative parameter observed was that of overall flame stability, which was marked by the degree of curvature at the edges of the flame and the consistency of flame structure. Mixtures with 15-20% H_2 demonstrated a large degree of curvature at the edges, reduced flame diameter, and high flame oscillation frequency. Inconstant flame structure leads to reduced combustion efficiency, increased NO_x emissions, and flameouts which result in loss of power [31]. The minimum required fuel-hydrogen mole fraction to produce a stable, 1-D flame was 0.25 for equivalence ratios ranging 0.8-1.1, with an inlet fuel/oxidizer velocity of 7.46 cm/s.

3.2 NO_x Measurements

3.2.1 Model Predictions

Pre-mixed, laminar burner stabilized combustion was simulated in Chemkin using the mechanism developed by [24] for $x_{H_2} = 0.15-0.50$, and $\phi = 1.0$. As shown in Chapter 2 regardless of the specific conditions, the model predicted that NO concentration saturates and plateaus ~ 2.5 mm above the burner surface. Figure 3.3 plots predictions of the NO concentration 15mm downstream (i.e. the maximum concentration) of the burner surface both decrease as a function of the hydrogen fraction for mixtures with and without N_2 . The NO level is essentially flat at ~ 5000 ppm with a slight decline with H_2 fraction, and the presence of N_2 has no influence.

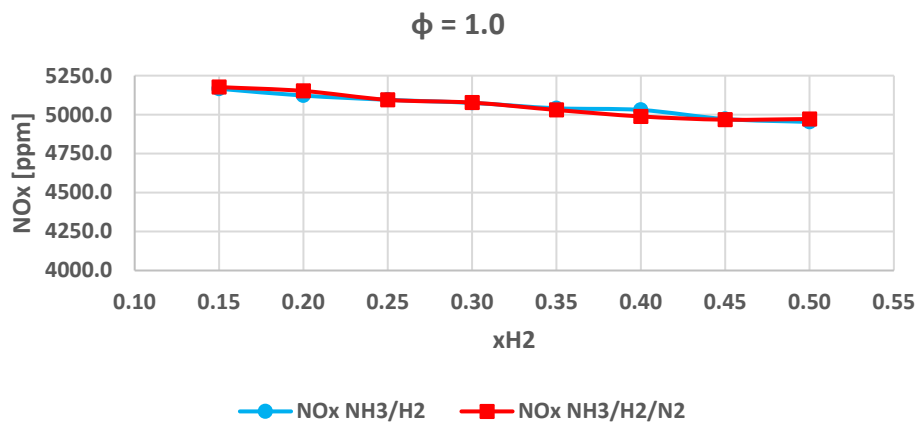


Figure 3.3 Model predictions NO_x concentration 15mm above the burner surface at $\phi = 1.0$, varying x_{H_2} .

Figure 3.4 shows the model predictions for how the maximum NO_x concentration varies as a function of equivalence ratio at $x_{H_2} = 0.3$. The model predicts insignificant differences in NO_x emissions between the two fuel mixtures, suggesting additional N₂ in NH₃/H₂/N₂ mixtures does not contribute to NO formation. Lean conditions produce higher NO_x whereas rich conditions produce lower NO_x, which is consistent with ammonia-combustions trends discussed in chapter 1.4.

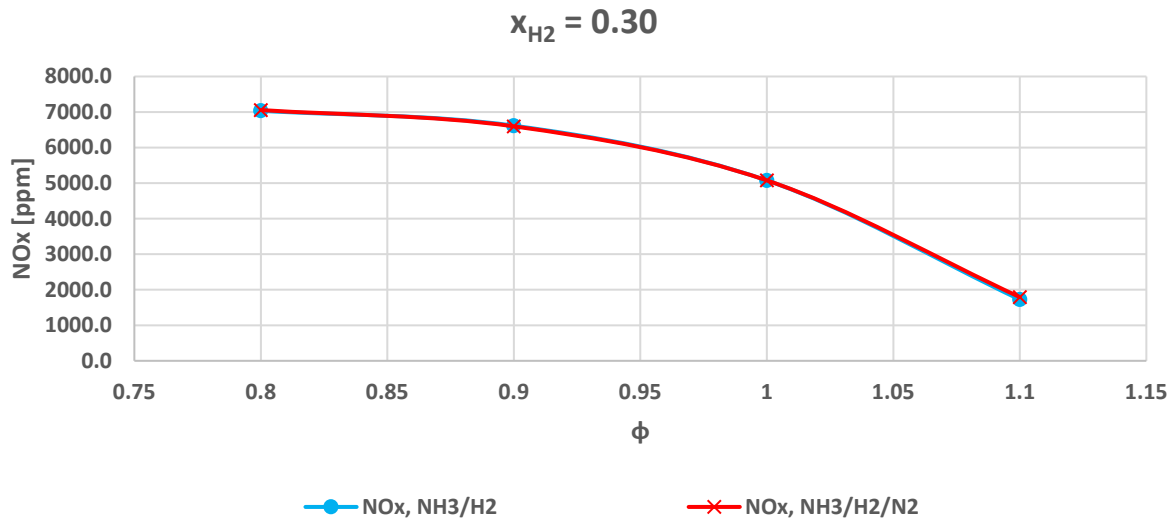


Figure 3.4 Model predictions of NO_x concentration for 30% hydrogen fuel mixtures as a function of equivalence ratio 15mm above the burner surface.

3.2.2 Experimental Results

3.2.2.1 Original NO_x Measurements

Initial NO_x measurements were completed before the modeling framework in Chemkin was performed. In these experiments the location of the sampling tube was varied and the results reported reflect the maximum NO_x measured, corrected to account for dilution from the shroud gas. Figure 3.5 compares the experimental maximum NO_x of the two mixtures across the range of operating conditions. The initial results strongly supported the hypothesis that additional N₂ increases NO_x emissions in ammonia-hydrogen fuel mixtures.

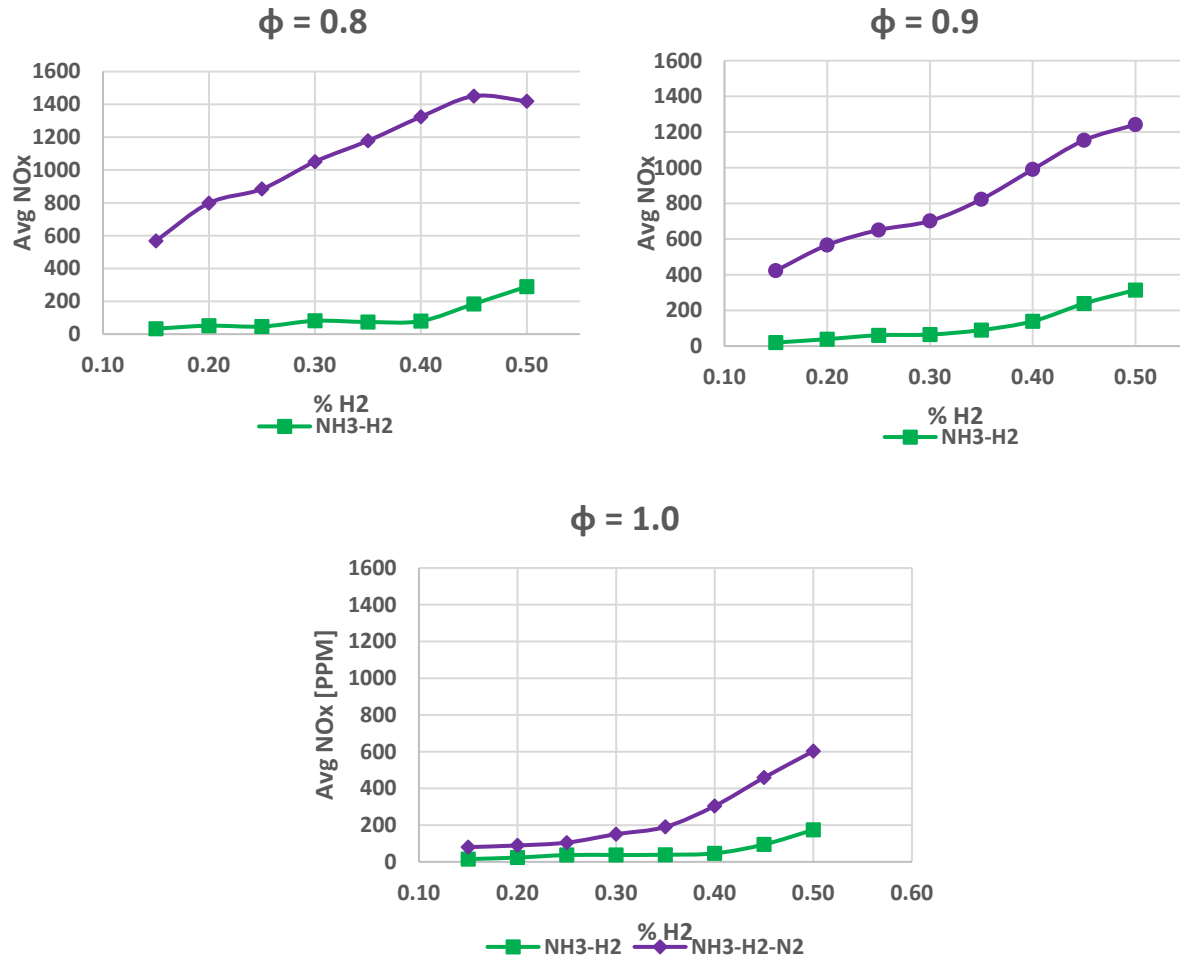


Figure 3.5 Average experimental NO_x concentrations of NH₃/H₂ mixtures compared to NH₃/H₂/N₂ mixtures at (a) $\phi = 0.8$, (b) $\phi = 0.9$, and (c) $\phi = 1.0$ as a function of x_{H_2} .

However, the initial results did not stand up to scrutiny against model predictions. Figure 3.6 compares the experimental maximum NO_x to the model predictions for 30% hydrogen fuel mixtures as a function of equivalence ratio. Quantitatively, the experimental results do not agree with the model predictions. The model predicts NO_x concentrations to be an order of magnitude greater than the experimental concentrations. In addition, the model shows no impact of N₂ addition, yet in the experiments the absence of N₂ created a significant NO_x reduction. However, qualitatively the model and experimental results have partial agreement in that the NO_x concentration decreased as equivalence ratio increased. Possible explanations for this disparity will be discussed in section 3.2.3.

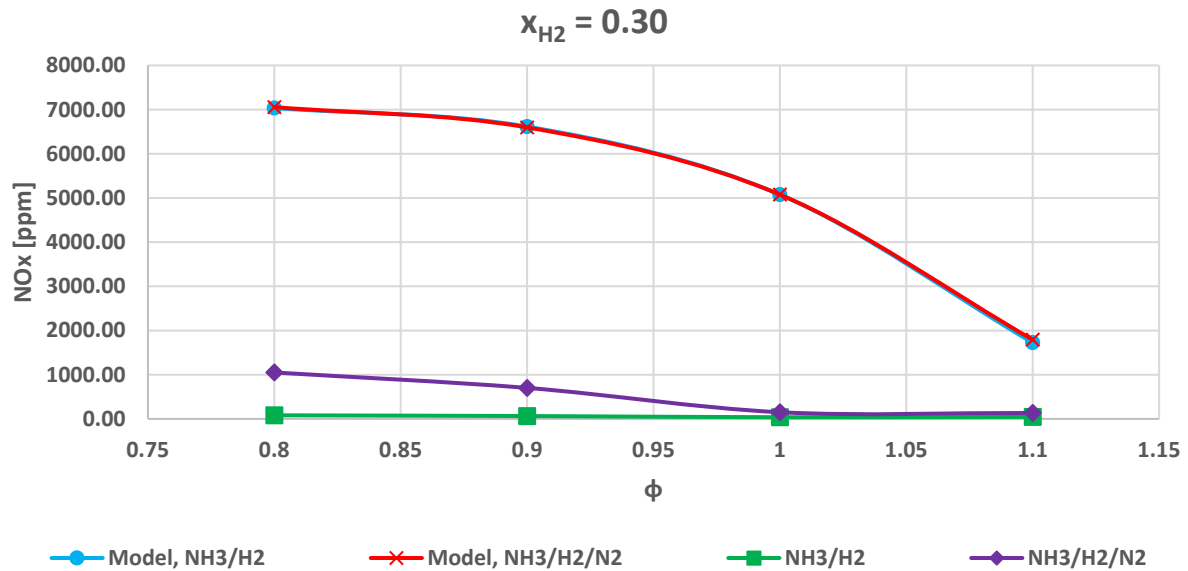


Figure 3.6 NO_x measurements of experimental (Exp) results compared to Chemkin (C) results for $x_{H_2} = 0.3$.

3.2.3 Challenges in Experimentation

A number of challenges arose throughout data collection that prevented a thorough investigation as to why the model and experimental results for NO_x emissions were quantitatively inconsistent compared to the model. Ammonia combustion produces a large amount of water, accounting for 30% of combustion products according to the Chemkin simulations. This was confirmed throughout experimentation as water condensation accumulated on the walls of the combustion chamber after ~10 minutes of operation. The volume of the chamber was much larger than the burner used, which created an environment where radiative heat loss was inevitable, resulting in a large degree of condensation within the chamber. At times the condensation was so extensive that the burner surface became saturated with water, rendering ignition impossible without opening the chamber and re-introducing atmospheric air to the interior. Better ventilation was necessary, but could not be achieved without introducing atmospheric oxygen to the chamber, which affected combustion conditions. For example, if atmospheric air entered the chamber while examining a fuel-lean flame, the flame stability increased due to the availability of oxygen from the air. Additionally, the presence of atmospheric air diluted the NO_x concentration to an indeterminable degree. This was evident in experiments in which the chamber was not fully purged of atmospheric air prior to combustion. When residual air was present in the chamber, the NO_x measurements would start at values in the range of 2000-3500 ppm. But as residual air depleted, the NO_x measurements would

gradually decrease to values below 900 ppm, and eventually below 100 ppm under constant combustion. It became clear that residual air in the chamber prevented excessive condensation, which improved the functionality of the NO_x analyzer, however at the expense of diluting the measurement.

Another complication was that throughout data collection, NO_x measurements for both blends progressively decreased and eventually were unrepeatable when the chamber was completely insulated. The earliest measurements recorded the highest NO_x concentrations, and the latest measurements recorded the lowest NO_x concentrations. This raised the question of why the measurements progressively decreased over time, despite performing routine maintenance and calibration on the NO_x analyzer. One possibility could be that combustion products accumulated in the sample tube over time, and impeded accurate measurements from the NO_x analyzer. However, when atmospheric air was introduced to the chamber during combustion, the NO_x measurement on the analyzer would immediately increase, indicating that the analyzer function was normal. Another explanation could be that an accumulation of unburned ammonia in the sampling tube enabled SCR or SCNR reactions.

The decline in NO_x concentrations over continued combustion was addressed with the following hypothesis: the NO_x analyzer measurements were lower than predicted values due to NO_x -reduction reactions occurring in the sampling tube. This hypothesis was tested by first determining whether the NO_x analyzer was functioning correctly. A calibration gas of 4000 ppm NO in N₂ was fed directly to the analyzer's input port, and the NO_x measured was within an acceptable range (3890-4011 ppm). Next the calibration gas was fed through the sample tube, and read expected values. A 30% NH₃/H₂ mixture flame was ignited in the chamber and burned for 10 minutes to saturate the sample tube with combustion products. Finally, the calibration gas was fed through the sample tube for a second time. Figure 3.7 shows the comparison between the NO_x analyzer measurements when the calibration gas was sent through the sampling tube pre and post combustion.

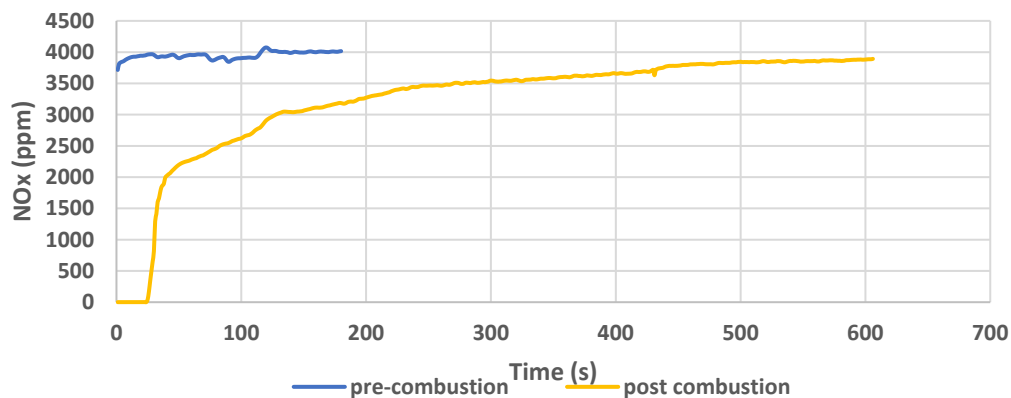


Figure 3.7 NO_x analyzer calibration gas measurements pre and post combustion operations.

The post-combustion curve deserves attention due to the gradual approach toward the calibration gas concentration / pre-combustion concentration. The results suggest that either combustion products coat the sampling tube in such a way that the NO_x analyzer is unable to perform accurate chemiluminescence; or unburned ammonia accumulates in the sample tube and reduces nitrogen oxides until either the ammonia is cleared out from the sample tube, or the NH₃:NO_x ratio is insufficient for reduction reactions to continue.

As described in chapter 1.4.3, SCR and SNCR describe the reactions between vaporized ammonia (the reagent) and NO to produce nitrogen and water. The difference between the two is the presence of a catalyst in SCR. The sample tube used in this work had an inert coating of SilcoNert 2000 on a 316-stainless steel support. This coating tolerates pH levels from 0-8, whereas water-ammonia mixtures have a pH of 11-12. According to the Siltek coating manufacturer, the mixture of water produced from combustion and any unburned ammonia likely etched the coating of the sample tube, especially under temperatures where steam is generated. It is possible that etches in the coating exposed the stainless steel support of the tube, which is often a base for catalysts used in SCR applications [32]. The conditions of the experiments (applying heat to the sample tube, the production of water through combustion, and the basic pH of NH₃/H₂O solutions) likely etched the inert coating, and created an environment in which SCR occurred in the sample tube.

Figure 3.7 demonstrated that the NO_x analyzer was indeed functioning properly when measuring dry gasses. What was not clear is did the presence of combustion products, particularly moisture, in the sampling tube lead to incorrect measurements or did these species contribute to NO_x reduction in the sampled gas? To resolve this issue a second NO_x detector, manufactured by Forensics DetectorsTM, was acquired (referred to as “NO_x detector”). The purpose of using a different NO_x detector was to determine whether NO_x reduction reactions were occurring within the sample tube or combustion chamber, or whether water vapor produced in ammonia combustion was impeding accurate NO_x measurements. The NO_x detector did not have a sampling line, but simply needed to be placed within the desired gas stream. The simplest and safest placement was at the end of the exhaust line at top of the exhaust flue (Figure 3.8). The NO_x analyzer sample tube was adjusted to take samples from the exhaust flue, midway between the top of the chamber and the end of the flue hose. In this experiment, data from the detector was inconclusive – NO_x measurements varied randomly from 100-3200 ppm without changing any of the combustion operating conditions, and the detector would get stuck reading a certain value, regardless of whether atmospheric air or combustion flue was being sampled. Measurements from the NO_x analyzer did not exceed 18 ppm, despite testing both mixtures across the range of ϕ and x_{H_2} . It became clear that after a duration of sampling combustion products, both the detector and analyzer reached a point of saturation that prevented accurate measurements.

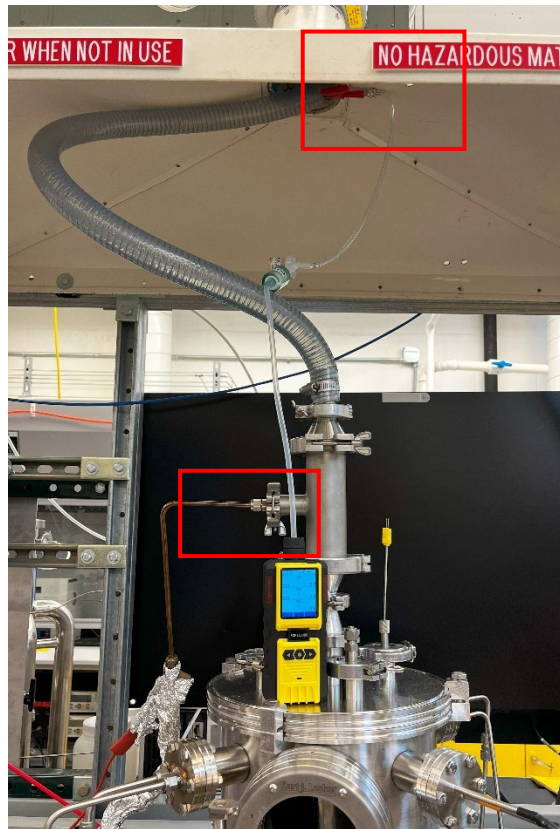


Figure 3.8 NO_x detector and NO_x analyzer sample tube location with emphasis on the detection and sample tube locations.

One way to mitigate saturating the devices was through increasing ventilation in the chamber. This was accomplished by allowing atmospheric air to diffuse through a 0.25 inch sampling port on the top of the chamber. The sampling port cap was removed after igniting the flame, and it was assumed that the shroud gas contained the combustion products within the center of the chamber to prevent escape to the external environment. Even this small amount of ventilation was sufficient to prevent condensation accumulation within the chamber. Another benefit associated with ventilation was smooth operations with the NO_x measuring equipment – neither displayed signs of saturation. This ventilation did not disrupt the flame, but diluted the exhaust with air. Unfortunately, the amount of air that diffused into the chamber was not measured so the degree of dilution is unknown.

Figure 3.9 compares the NO_x measurements from the NO_x detector and the NO_x analyzer under this updated configuration (sampling from the flue stack with chamber ventilation) across the range of operating conditions. The detector measured NO_x concentrations that were on average 1.79-2.23 times greater than the analyzer measurements. The ventilation occurred downstream of both sampling positions, so the gas composition should have nominally been very similar. Based on the results, it is suspected that

additional NO_x reduction is still occurring in the sampling line to the analyzer, with the amount of NO_x being consumed indicated by the multiplicative difference in measurements.

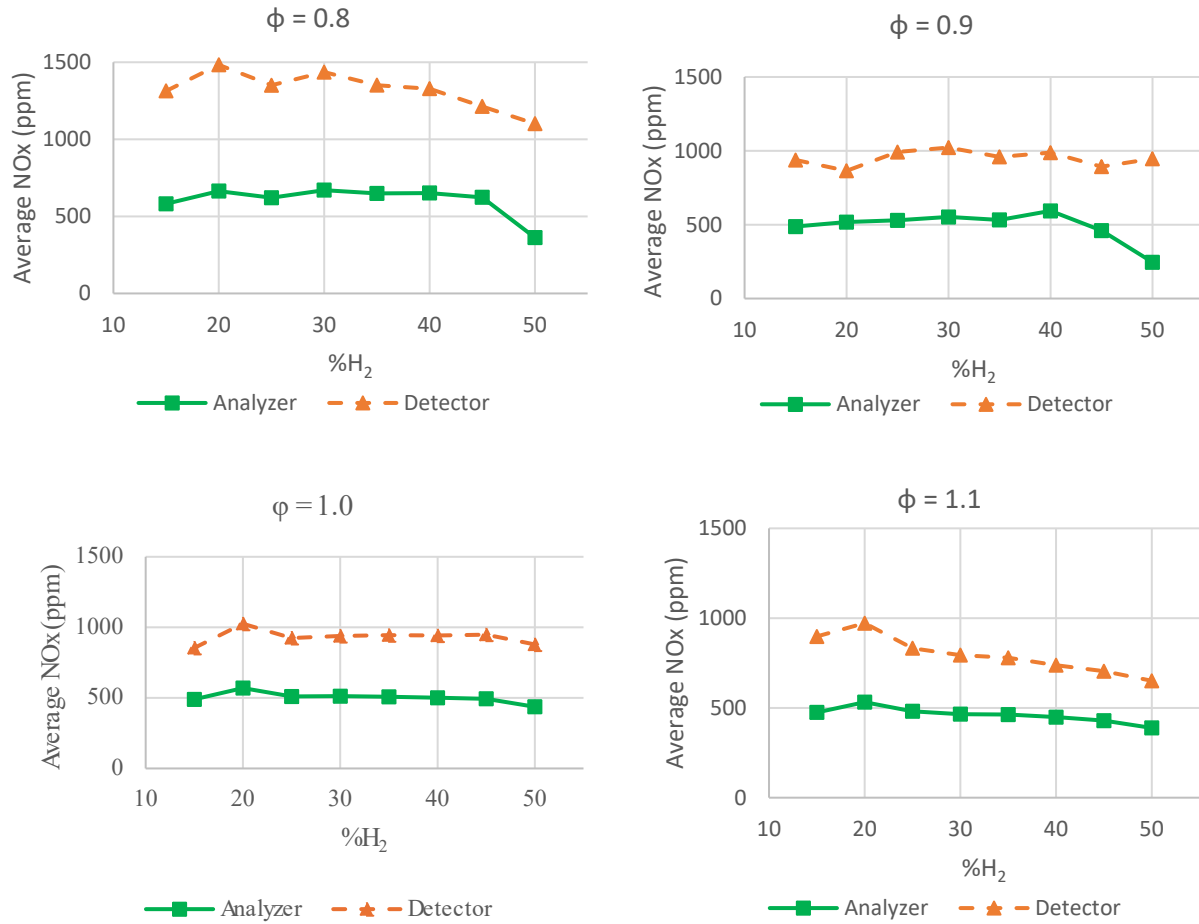


Figure 3.9 Comparison of NO_x measurements between the NO_x analyzer and NO_x detector across the range of operating conditions for the NH₃/H₂ mixture, with chamber ventilation.

Nevertheless the experiments with chamber ventilation were more consistent with the model predictions, both qualitatively and quantitatively. First the NO_x levels are ~ 1000 ppm (with the detector), much more reasonable values. Note that in comparison to the flame predictions, the experiment is diluted both by the shroud gas as well as the additional air used to ventilate the chamber. Second, the NO_x levels gradually decline with increasing hydrogen fraction, in good agreement with model prediction (refer to Figure 3.3). In addition NO_x decreased as the equivalence ratio increased.

3.2.3.1 Updated Experimental NO_x Measurements

After addressing the issue of excessive condensation and confirming the reliability of the NO_x analyzer measurements, experiments were repeated with the modification of allowing chamber ventilation. The experimental results measuring NO_x across the range of flat flame conditions for $\phi = 0.8-1.1$ are compared in Figure 3.10. Two findings were consistent across experimental results: NH₃/H₂ and NH₃/H₂/N₂ mixtures produced the same NO_x concentrations within a ~10% variance, and NO_x formation slightly decreased as x_{H_2} increased. Both findings are consistent with the model predictions that there is a negligible difference in NO_x produced between the two mixtures, and there is an inverse relationship between NO_x formation and x_{H_2} .

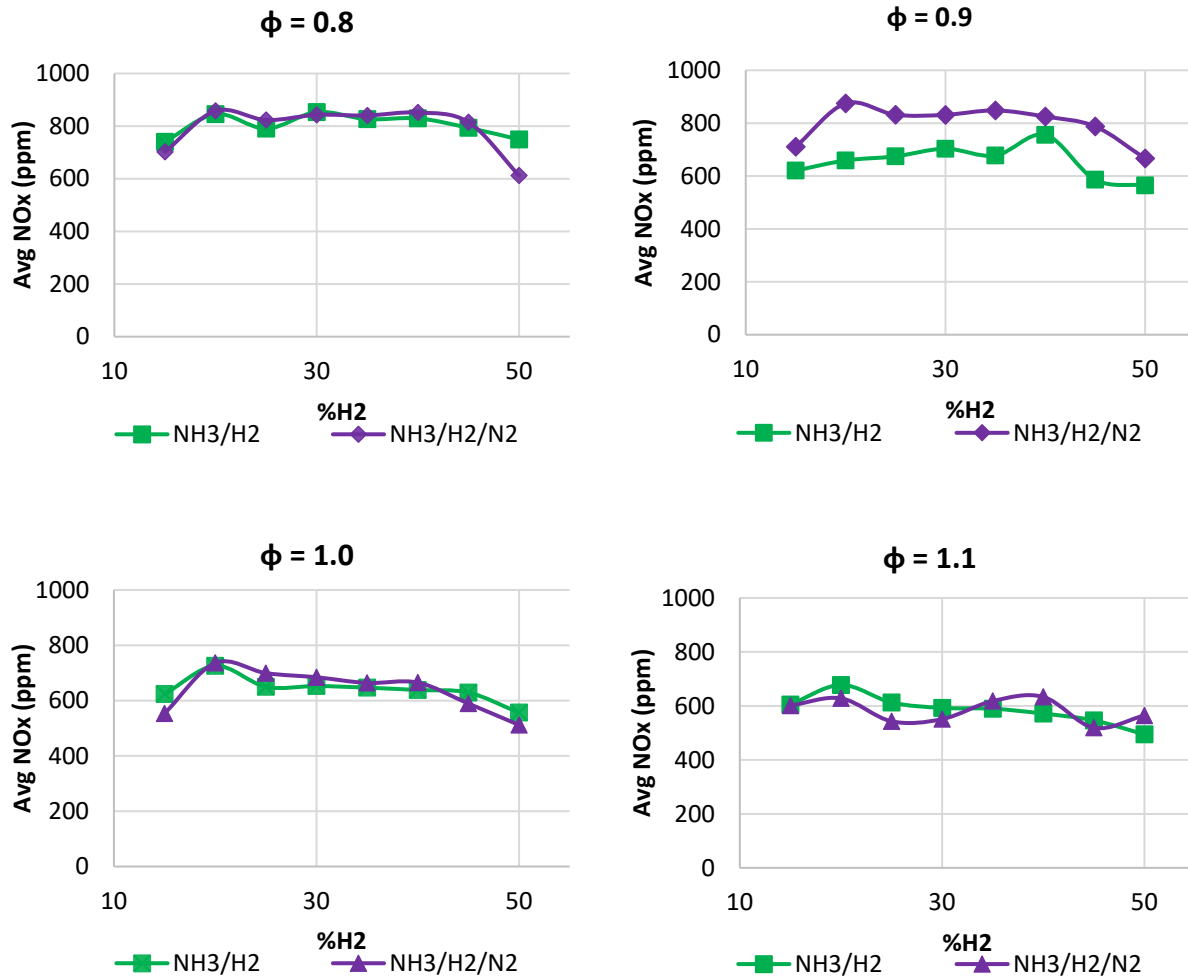


Figure 3.10 Comparison of NO_x emissions between NH₃/H₂ and NH₃/H₂/N₂ flames with NO_x analyzer and chamber ventilation.

Figure 3.11 compares the model and experimental results from both analyzers with chamber ventilation. Experimental results demonstrated that NO_x measurements for both mixtures were often an order of magnitude less than model predictions. This could be attributed to the dilution of the sample from the addition of atmospheric air to the combustion chamber. Figure 3.12 demonstrates the same order of magnitude disparity for $\phi = 1.0$ and $x_{\text{H}_2} = 0.15-0.50$. However, the relationship between NO_x and x_{H_2} is in very good agreement with model predictions.

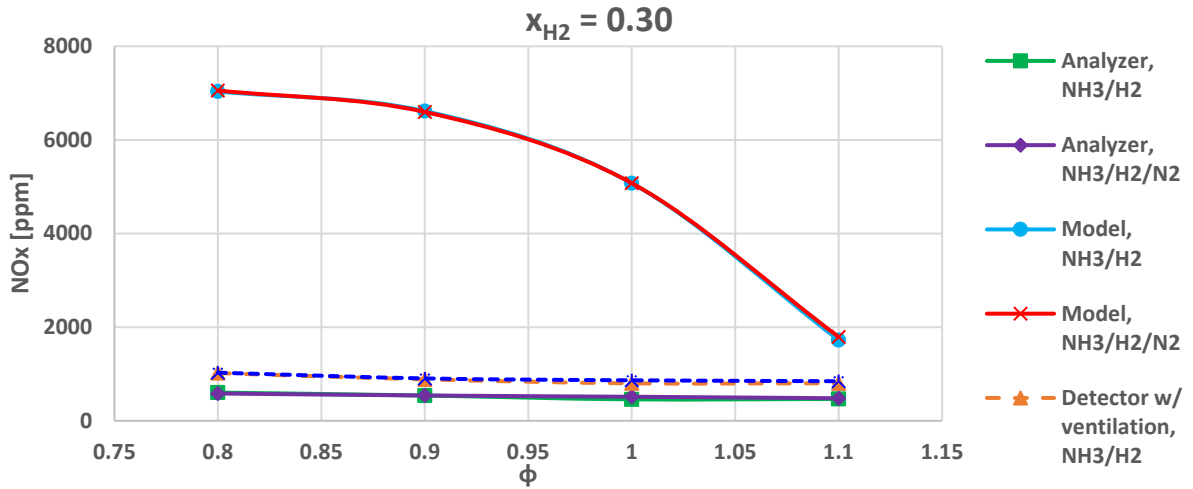


Figure 3.11 NO_x measurements of experimental (Exp) results compared to Chemkin (C) results for $x_{\text{H}_2} = 0.3$.

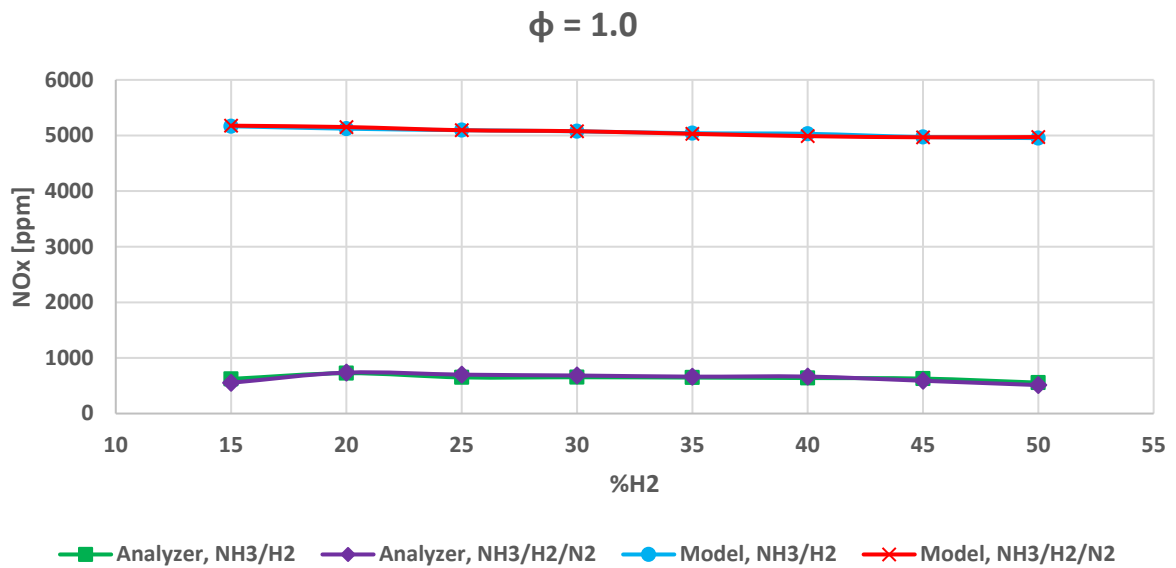


Figure 3.12 Comparison of model predictions and experimental results of NO_x for $\phi = 1.0$, $x_{\text{H}_2} = 0.15-50$ for both NH_3/H_2 and $\text{NH}_3/\text{H}_2/\text{N}_2$ mixtures.

4.1 Conclusions

The purpose of this study was to analyze nitrogen oxide emissions of cracked-ammonia fuel mixtures. NH_3/H_2 and $\text{NH}_3/\text{H}_2/\text{N}_2$ mixtures were compared at a range of equivalence ratio (0.8-1.1) and fuel-hydrogen mole fraction (0.15-50) both computationally and experimentally. The following conclusions summarize the current status of NO_x production characterization in laminar, burner-stabilized ammonia/hydrogen combustion.

4.1.1 Flame Stability

The range of operating conditions at which stable, 1-dimensional flames are obtained was defined. Fuel mixtures with additional N_2 demonstrated lower flame stability at $x_{\text{H}_2} \leq 0.20$, and experienced slower ignition. Increasing the fuel-hydrogen mole fraction in either mixture resulted in increased stability.

4.1.2 NO_x Production

This research demonstrated that there is an insignificant difference between the NO_x produced in NH_3/H_2 and $\text{NH}_3/\text{H}_2/\text{N}_2$ mixtures in burner-stabilized combustion at atmospheric pressure. In this regard, the experimental results demonstrated qualitative agreement with the model. However, the concentrations in the model were ~ 10 times higher than the experimental measurements. The primary issue that was learned, unfortunately late in this thesis, is that both NO_x detectors employed fail under the high humidity levels. They appear to become saturated with moisture rendering any measurements incorrect. In the case of the analyzer it was demonstrated that in the presence of combustion products it appears that NO_x is at least partially reduced in the sampling line, likely through some type of SCR chemistry. Interestingly, model predictions identified significant quantities of H, OH, and unburned H_2 in the flame exhaust. These species could potentially contribute to the SCR downstream, in addition to the likely occurrence of etching and exposing a catalytic surface in the sample tube interior. The possibility of SCR was further supported by comparing the NO_x measurements with two analyzers. The NO_x detector reporting concentrations 1.79-2.23 times greater than the analyzer measurements suggests that 39-70% of the NO_x produced is reduced in the sample tube.

In order to obtain reproducible measurements it was necessary to dilute the exhaust with an unknown amount of air to prevent condensation and achieve reproducible measurements that were considered qualitatively if not quantitatively correct. While the dilution limited the accuracy of the results, the primary question comparing NO_x production between cracked ammonia mixtures was answered. The

results in this work also raise the question of how much NO_x emissions can be reduced in the presence of ammonia-combustion products.

4.2 Recommendations

The following recommendations are proposed to improve cracked-ammonia fuel NO_x characterization and areas of further study.

There were several challenges that prevented a quantitative characterization of NO_x production from cracked-ammonia fuels. One challenge was the amount of water produced in ammonia-hydrogen combustion. Insulating the combustion chamber from the external environment resulted in high levels of condensation build-up in the chamber, which became a serious concern. While insulation was desired in creating a controlled environment in which reactive species' quantities were known, it came at the expense of saturating the NO_x measurement equipment and producing “sticky” readings. Furthermore, ammonia-water solutions likely degraded the inert coating of the sampling tube, introducing the possibility of SCR. Three approaches should be taken to address these challenges: (1) deliver a known flow rate (via a mass flow controller) of a dilution gas to the chamber to reduce condensation and improve analyzer functionality. This would enable the determination of the required flow to prevent condensation, and accurate accounting for dilution; (2) feed the analyzer with a humidified calibration gas to determine the humidity at which the analyzer performance degrades; (3) use a sampling tube with a coating that can withstand higher pH and temperatures such as quartz, and compare NO_x measurements to determine the presence and or extent of SCR.

There are a number of variables that were not studied in this work, but could provide insights into the differences between NH_3/H_2 and $\text{NH}_3/\text{H}_2/\text{N}_2$ mixtures. Extending this study at elevated pressures would be a logical next-step as compression engines operate at higher pressure. Future studies should apply focus to determining the amount of ammonia-slip across the range of operating conditions. Measuring unburned ammonia would be important in addressing whether there is enough slip to enable SCR, and inform the trade-off between operating at higher equivalence ratios, which produces less NO_x , but likely results in greater slip. Preheating the unburned fuel also deserves attention, as hotter fuels produce less condensation and observe higher laminar flame speed.

REFERENCES

- [1] P. Berwal, S. Kumar, and B. Khandelwal, 'A comprehensive review on synthesis, chemical kinetics, and practical application of ammonia as future fuel for combustion', *Journal of the Energy Institute*, vol. 99. Elsevier B.V., pp. 273–298, Dec. 01, 2021. doi: 10.1016/j.joei.2021.10.001.
- [2] W. S. Chai, Y. Bao, P. Jin, G. Tang, and L. Zhou, 'A review on ammonia, ammonia-hydrogen and ammonia-methane fuels', *Renewable and Sustainable Energy Reviews*, vol. 147. Elsevier Ltd, Sep. 01, 2021. doi: 10.1016/j.rser.2021.111254.
- [3] I. Rolo, V. A. F. Costa, and F. P. Brito, 'Hydrogen-Based Energy Systems: Current Technology Development Status, Opportunities and Challenges', *Energies*, vol. 17, no. 1. Multidisciplinary Digital Publishing Institute (MDPI), Jan. 01, 2024. doi: 10.3390/en17010180.
- [4] M. Yu, K. Wang, and H. Vredenburg, 'Insights into low-carbon hydrogen production methods: Green, blue and aqua hydrogen', *Int J Hydrogen Energy*, vol. 46, no. 41, pp. 21261–21273, Jun. 2021, doi: 10.1016/j.ijhydene.2021.04.016.
- [5] H. Kobayashi, A. Hayakawa, K. D. K. A. Somarathne, and E. C. Okafor, 'Science and technology of ammonia combustion', *Proceedings of the Combustion Institute*, vol. 37, no. 1, pp. 109–133, 2019, doi: 10.1016/j.proci.2018.09.029.
- [6] A. Valera-Medina *et al.*, 'Review on ammonia as a potential fuel: From synthesis to economics', *Energy and Fuels*, vol. 35, no. 9. American Chemical Society, pp. 6964–7029, May 06, 2021. doi: 10.1021/acs.energyfuels.0c03685.
- [7] P. Berwal, S. Kumar, and B. Khandelwal, 'A comprehensive review on synthesis, chemical kinetics, and practical application of ammonia as future fuel for combustion', *Journal of the Energy Institute*, vol. 99. Elsevier B.V., pp. 273–298, Dec. 01, 2021. doi: 10.1016/j.joei.2021.10.001.
- [8] M. Comotti and S. Frigo, 'Hydrogen generation system for ammonia-hydrogen fuelled internal combustion engines', *Int J Hydrogen Energy*, vol. 40, no. 33, pp. 10673–10686, Sep. 2015, doi: 10.1016/j.ijhydene.2015.06.080.
- [9] F. B. Juangsa, P. S. Darmanto, and M. Aziz, 'CO₂-free power generation employing integrated ammonia decomposition and hydrogen combustion-based combined cycle', *Thermal Science and Engineering Progress*, vol. 19, Oct. 2020, doi: 10.1016/j.tsep.2020.100672.
- [10] Z. Zhang, S. Liguori, T. F. Fuerst, J. D. Way, and C. A. Wolden, 'Efficient Ammonia Decomposition in a Catalytic Membrane Reactor to Enable Hydrogen Storage and Utilization', *ACS Sustain Chem Eng*, vol. 7, no. 6, pp. 5975–5985, Mar. 2019, doi: 10.1021/acssuschemeng.8b06065.
- [11] R. Sitar, J. Shah, J. D. Way, and C. A. Wolden, 'Efficient Generation of H₂/NH₃Fuel Mixtures for Clean Combustion', *Energy and Fuels*, vol. 36, no. 16, pp. 9357–9364, Aug. 2022, doi: 10.1021/acs.energyfuels.2c01822.
- [12] W. S. Chai, Y. Bao, P. Jin, G. Tang, and L. Zhou, 'A review on ammonia, ammonia-hydrogen and ammonia-methane fuels', *Renewable and Sustainable Energy Reviews*, vol. 147. Elsevier Ltd, Sep. 01, 2021. doi: 10.1016/j.rser.2021.111254.
- [13] A. A *et al.*, 'Evolution of ammonia reaction mechanisms and modeling parameters: A review', *Applications in Energy and Combustion Science*, vol. 15, Sep. 2023, doi: 10.1016/j.jaecs.2023.100175.

- [14] T. Cai, D. Zhao, S. H. Chan, and M. Shahsavari, ‘Tailoring reduced mechanisms for predicting flame propagation and ignition characteristics in ammonia and ammonia/hydrogen mixtures’, *Energy*, vol. 260, Dec. 2022, doi: 10.1016/j.energy.2022.125090.
- [15] J. Chen, X. Jiang, X. Qin, and Z. Huang, ‘Effect of hydrogen blending on the high temperature auto-ignition of ammonia at elevated pressure’, *Fuel*, vol. 287, Mar. 2021, doi: 10.1016/j.fuel.2020.119563.
- [16] C. Duynslaegher, F. Contino, J. Vandooren, and H. Jeanmart, ‘Modeling of ammonia combustion at low pressure’, *Combust Flame*, vol. 159, no. 9, pp. 2799–2805, Sep. 2012, doi: 10.1016/j.combustflame.2012.06.003.
- [17] F. R. Westlye, A. Ivarsson, and J. Schramm, ‘Experimental investigation of nitrogen based emissions from an ammonia fueled SI-engine’, *Fuel*, vol. 111, pp. 239–247, 2013, doi: 10.1016/j.fuel.2013.03.055.
- [18] G. G. De Soete, ‘OVERALL REACTION RATES OF NO AND N_x FORMATION FROM FUEL NITROGEN’.
- [19] C. Netzer, A. Ahmed, A. Gruber, and T. Løvås, ‘Curvature effects on NO formation in wrinkled laminar ammonia/hydrogen/nitrogen-air premixed flames’, *Combust Flame*, vol. 232, Oct. 2021, doi: 10.1016/j.combustflame.2021.111520.
- [20] A. HAYAKAWA, T. GOTO, R. MIMOTO, T. KUDO, and H. KOBAYASHI, ‘NO formation/reduction mechanisms of ammonia/air premixed flames at various equivalence ratios and pressures’, *Mechanical Engineering Journal*, vol. 2, no. 1, pp. 14-00402-14-00402, 2015, doi: 10.1299/mej.14-00402.
- [21] R. C. Rocha, M. Costa, and X.-S. Bai, ‘Combustion and Emission Characteristics of Ammonia under Conditions Relevant to Modern Gas Turbines’, *Combustion Science and Technology*, vol. 193, no. 14, pp. 2514–2533, Oct. 2021, doi: 10.1080/00102202.2020.1748018.
- [22] B. G. Miller, ‘Emissions Control Strategies for Power Plants’, in *Clean Coal Engineering Technology*, Elsevier, 2011, pp. 375–481. doi: 10.1016/b978-1-85617-710-8.00009-1.
- [23] A. Goldmann and F. Dinkelacker, ‘Approximation of laminar flame characteristics on premixed ammonia/hydrogen/nitrogen/air mixtures at elevated temperatures and pressures’, *Fuel*, vol. 224, pp. 366–378, Jul. 2018, doi: 10.1016/j.fuel.2018.03.030.
- [24] X. Meng *et al.*, ‘Investigation of ammonia cracking combined with lean-burn operation for zero-carbon combustion and NO/N₂O/NO₂ improvements’, *J Clean Prod*, vol. 428, Nov. 2023, doi: 10.1016/j.jclepro.2023.139478.
- [25] S. Frigo and R. Gentili, ‘Analysis of the behaviour of a 4-stroke Si engine fuelled with ammonia and hydrogen’, *Int J Hydrogen Energy*, vol. 38, no. 3, pp. 1607–1615, Feb. 2013, doi: 10.1016/j.ijhydene.2012.10.114.
- [26] M. Comotti and S. Frigo, ‘Hydrogen generation system for ammonia-hydrogen fuelled internal combustion engines’, *Int J Hydrogen Energy*, vol. 40, no. 33, pp. 10673–10686, Sep. 2015, doi: 10.1016/j.ijhydene.2015.06.080.
- [27] M. Comotti and S. Frigo, ‘Hydrogen generation system for ammonia–hydrogen fuelled internal combustion engines’, *Int J Hydrogen Energy*, vol. 40, no. 33, pp. 10673–10686, Sep. 2015, doi: 10.1016/J.IJHYDENE.2015.06.080.
- [28] ‘Holthuis and Associates Flat Flame Burner’, 2022.
- [29] ‘nCLD-Operating-Manual-EN-0519 2019 (1)’.

- [30] C. Bedick, 'Status of Ammonia Combustion Research at NETL', May 2023.
- [31] W. Xu, Y. Yan, G. Lu, and X. Bai, 'Quantitative Assessment of Burner Flame Stability Through Digital Image Processing', *IEEE Trans Instrum Meas*, vol. 71, 2022, doi: 10.1109/TIM.2022.3205671.
- [32] W. Wang, S. Zhao, X. Tang, C. Chen, and H. Yi, 'Stainless steel catalyst for air pollution control: structure, properties, and activity', *Environmental Science and Pollution Research*, vol. 29, no. 37. Springer Science and Business Media Deutschland GmbH, pp. 55367–55399, Aug. 01, 2022. doi: 10.1007/s11356-022-21079-z.

APPENDIX A EXPERIMENTAL SPECIFICATIONS

Table A.1 Component Volumetric flow rates (SLM) used for NH₃/H₂ and NH₃/H₂/N₂ mixtures, across the range of operating conditions ($\phi = 0.8-1.1$, $x_{H_2} = 0.10-0.50$).

NH ₃ /H ₂						
ϕ	%H ₂	%NH ₃	Q _{H2}	Q _{NH3}	Q _{Air}	Q _{Ar}
0.8	10	90	0.043	0.389	1.765	0.601
	15	85	0.066	0.374	1.757	0.601
	20	80	0.090	0.358	1.750	0.601
	25	75	0.114	0.342	1.741	0.601
	30	70	0.139	0.325	1.733	0.601
	35	65	0.166	0.308	1.724	0.601
	40	60	0.193	0.289	1.715	0.601
	45	55	0.221	0.270	1.706	0.601
	50	50	0.251	0.251	1.696	0.601
NH ₃ /H ₂ /N ₂						
ϕ	%H ₂	%NH ₃	Q _{H2/N2}	Q _{NH3}	Q _{Air}	Q _{Ar}
0.8	10	90	0.058	0.389	1.765	0.605
	15	85	0.088	0.374	1.757	0.607
	20	80	0.119	0.358	1.750	0.609
	25	75	0.152	0.342	1.741	0.612
	30	70	0.186	0.325	1.733	0.614
	35	65	0.221	0.308	1.724	0.616
	40	60	0.257	0.289	1.715	0.619
	45	55	0.295	0.270	1.706	0.621
	50	50	0.334	0.251	1.696	0.624

Table A.1 Continued

NH ₃ /H ₂						
φ	%H ₂	%NH ₃	Q _{H₂}	Q _{NH₃}	Q _{Air}	Q _{Ar}
0.9	10	90	0.044	0.397	1.756	0.601
	15	85	0.067	0.382	1.749	0.601
	20	80	0.091	0.365	1.741	0.601
	25	75	0.116	0.349	1.732	0.601
	30	70	0.142	0.332	1.724	0.601
	35	65	0.169	0.314	1.715	0.601
	40	60	0.197	0.295	1.705	0.601
	45	55	0.226	0.276	1.696	0.601
	50	50	0.256	0.256	1.686	0.601
NH ₃ /H ₂ /N ₂						
φ	%H ₂	%NH ₃	Q _{H₂/N₂}	Q _{NH₃}	Q _{Air}	Q _{Ar}
0.9	10	90	0.059	0.389	1.756	0.603
	15	85	0.090	0.374	1.749	0.605
	20	80	0.122	0.358	1.741	0.608
	25	75	0.155	0.342	1.732	0.610
	30	70	0.190	0.325	1.724	0.612
	35	65	0.225	0.308	1.715	0.615
	40	60	0.262	0.289	1.705	0.618
	45	55	0.301	0.270	1.696	0.620
	50	50	0.341	0.251	1.686	0.623

Table A.1 Continued

NH ₃ /H ₂						
φ	%H ₂	%NH ₃	Q _{H₂}	Q _{NH₃}	Q _{Air}	Q _{Ar}
1.0	10	90	0.045	0.404	1.749	0.601
	15	85	0.068	0.388	1.741	0.601
	20	80	0.093	0.371	1.733	0.601
	25	75	0.118	0.355	1.725	0.601
	30	70	0.144	0.337	1.716	0.601
	35	65	0.172	0.319	1.707	0.601
	40	60	0.200	0.300	1.697	0.601
	45	55	0.229	0.280	1.687	0.601
	50	50	0.260	0.260	1.677	0.601
NH ₃ /H ₂ /N ₂						
φ	%H ₂	%NH ₃	Q _{H₂/N₂}	Q _{NH₃}	Q _{Air}	Q _{Ar}
1.0	10	90	0.060	0.404	1.749	0.605
	15	85	0.091	0.388	1.741	0.607
	20	80	0.124	0.371	1.733	0.610
	25	75	0.158	0.355	1.725	0.612
	30	70	0.193	0.337	1.716	0.614
	35	65	0.229	0.319	1.707	0.617
	40	60	0.267	0.300	1.697	0.619
	45	55	0.306	0.280	1.687	0.622
	50	50	0.347	0.260	1.677	0.625

Table A.1 Continued

NH ₃ /H ₂						
φ	%H ₂	%NH ₃	Q _{H₂}	Q _{NH₃}	Q _{Air}	Q _{Ar}
1.1	10	90	0.045	0.409	1.743	0.601
	15	85	0.069	0.393	1.735	0.601
	20	80	0.094	0.377	1.727	0.601
	25	75	0.120	0.359	1.718	0.601
	30	70	0.146	0.342	1.709	0.601
	35	65	0.174	0.323	1.700	0.601
	40	60	0.203	0.304	1.690	0.601
	45	55	0.233	0.284	1.681	0.601
	50	50	0.264	0.264	1.670	0.601
NH ₃ /H ₂ /N ₂						
φ	%H ₂	%NH ₃	Q _{H₂/N₂}	Q _{NH₃}	Q _{Air}	Q _{Ar}
1.1	10	90	0.061	0.404	1.743	0.604
	15	85	0.092	0.388	1.735	0.606
	20	80	0.126	0.371	1.727	0.608
	25	75	0.160	0.355	1.718	0.611
	30	70	0.195	0.337	1.709	0.613
	35	65	0.232	0.319	1.700	0.616
	40	60	0.270	0.300	1.690	0.619
	45	55	0.310	0.280	1.681	0.621
	50	50	0.351	0.260	1.670	0.624

APPENDIX B CHEMKIN INPUTS

Table B.2 Entries for the Chemkin Premixed Burner Code for $\phi = 1.0$.

NH ₃ /H ₂				NH ₃ /H ₂ /N ₂				
% H ₂	x _{H2}	x _{NH3}	Q _T	% H ₂	x _{H2}	x _{NH3}	x _{N2}	Q _T
10	0.1	0.9	447.527	10	0.09677	0.87097	0.03226	450.571
15	0.15	0.85	447.527	15	0.14286	0.80952	0.04762	452.173
20	0.2	0.8	447.527	20	0.1875	0.75	0.0625	453.832
25	0.25	0.75	447.527	25	0.23077	0.69231	0.07692	455.552
30	0.3	0.7	447.527	30	0.27273	0.63636	0.09091	457.335
35	0.35	0.65	447.527	35	0.31343	0.58209	0.10448	459.186
40	0.4	0.6	447.527	40	0.35294	0.52941	0.11765	461.107
45	0.45	0.55	447.527	45	0.3913	0.47826	0.13043	463.10
50	0.5	0.5	447.527	50	0.42857	0.42857	0.14286	465.181

Table B.3 Chemkin Outputs for Adiabatic Flame Temperatures using the Equilibrium Code for $\phi = 1.0$.

Fuel Mixture	NH ₃ /H ₂				NH ₃ /H ₂ /N ₂			
	Distance (cm)		Temperature		Distance (cm)		Temperature	
% H ₂	Start	End	Start	End	Start	End	Start	End
15	0	1.5	313	2110.96	0	1.5	313	2097.91
20	0	1.5	313	2122.95	0	1.5	313	2105.11
25	0	1.5	313	2122.95	0	1.5	313	2105.11
30	0	2.5	313	2147.91	0	2.5	313	2120.17
35	0	2.5	313	2161.01	0	2.5	313	2128.04
40	0	2.5	313	2174.55	0	2.5	313	2136.20
45	0	3.0	313	2188.54	0	3.0	313	2144.59
50	0	3.0	313	2202.99	0	3.0	313	2153.23

Table B.4 Chemkin “Solve Gas Energy Equation” Parameter Values

Parameter	Value
Maximum number of Grid Points Allowed	500
Number of Adaptive Grid Points	50
Adaptive Grid Control Based on Solution Gradient	0.2
Adaptive Grid Control Based on Solution Curvature	0.2
Starting Axial Position (cm)	0.0
Ending Axial Position (cm)	1.5
Number of Uniform Grid Points	300

APPENDIX C PYTHON SCRIPT FOR GOLDMAN'S CORRELATION EQUATIONS

```
# -*- coding: utf-8 -*-
```

```
"""
```

```
Created on Fri Apr 28 08:06:56 2023
```

```
@author: esmot
```

```
"""
```

```
# NH3/H2/Air Mixture Laminar Burning Velocities
```

```
# P is in MPa
```

```
# T is in K
```

```
# returns LBV in m/s, cm/s in the plots
```

```
import numpy as np
```

```
import math
```

```
import pandas as pd
```

```
from decimal import Decimal, getcontext
```

```
import matplotlib.pyplot as plt
```

```
co = pd.read_excel(r'Correlation_Coefficients.xlsx')
```

```
coeff = np.array(co, dtype=Decimal)
```

```
a10 = coeff[3,1:5]
```

```
a11 = coeff[4,1:5]
```

```
a12 = coeff[5,1:5]
```

```
a13 = coeff[6,1:5]
```

```
b10 = coeff[7,1:5]
```

```
b11 = coeff[8,1:5]
```

```
b12 = coeff[9,1:5]
```

```
b13 = coeff[10,1:5]
```

```
b14 = coeff[11,1:5]
```

```
c10 = coeff[12,1:5]
```

c11 = coeff[13,1:5]
c12 = coeff[14,1:5]
c13 = coeff[15,1:5]
c14 = coeff[16,1:5]
d10 = coeff[17,1:5]
d11 = coeff[18,1:5]
d12 = coeff[19,1:5]
d13 = coeff[20,1:5]
d14 = coeff[21,1:5]
a20 = coeff[23,1:5]
a21 = coeff[24,1:5]
a22 = coeff[25,1:5]
a23 = coeff[26,1:5]
b20 = coeff[27,1:5]
b21 = coeff[28,1:5]
b22 = coeff[29,1:5]
b23 = coeff[30,1:5]
c20 = coeff[31,1:5]
c21 = coeff[32,1:5]
c22 = coeff[33,1:5]
c23 = coeff[34,1:5]
d20 = coeff[35,1:5]
d21 = coeff[36,1:5]
d22 = coeff[37,1:5]
d23 = coeff[38,1:5]
a30 = coeff[40,1:5]
a31 = coeff[41,1:5]
a32 = coeff[42,1:5]
a33 = coeff[41,1:5]
b30 = coeff[44,1:5]
b31 = coeff[45,1:5]
b32 = coeff[46,1:5]
b33 = coeff[47,1:5]
c30 = coeff[48,1:5]

```

c31 = coeff[49,1:5]
c32 = coeff[50,1:5]
c33 = coeff[51,1:5]
d30 = coeff[52,1:5]
d31 = coeff[53,1:5]
d32 = coeff[54,1:5]
d33 = coeff[55,1:5]
e30 = coeff[56,1:5]
e31 = coeff[57,1:5]
e32 = coeff[58,1:5]
k1 = coeff[60,1]
k2 = coeff[61,1]
k3 = coeff[62,1]
k4 = coeff[63,1]

```

```

def param(xh2, l_row, p_index, temperature, pressure):

```

```

    qkn = 0

```

```

    if (temperature <= 700) and (pressure <= 0.5):

```

```

        if xh2 == 0:

```

```

            qkn = coeff[l_row,1]

```

```

        else:

```

```

            for i in range (0, p_index+1):

```

```

                qkn += coeff[l_row+i,1] * xh2**i

```

```

            #print(qkn)

```

```

    elif (temperature > 700) and (pressure <= 0.5):

```

```

        if xh2 == 0:

```

```

            qkn = coeff[l_row,2]

```

```

        else:

```

```

            for i in range (0, p_index+1):

```

```

                qkn += coeff[l_row+i,2] * xh2**i

```

```

            #print(qkn)

```

```

elif (temperature <= 800) and (pressure > 0.5):
    if xh2 == 0:
        qkn = coeff[l_row,3]
    else:
        for i in range (0, p_index+1):
            qkn += coeff[l_row+i,3] * xh2**i
        #print(qkn)

elif (temperature > 800) and (pressure > 0.5):
    if xh2 == 0:
        qkn = coeff[l_row,4]
    else:
        for i in range (0, p_index+1):
            qkn += coeff[l_row+i,4] * xh2**i
        #print(qkn)
else:
    print('Invalid temperature and pressure specified')

#print(qkn)
return qkn

# a1p2 = param(0.1, 3, 3, 293, 0.101324)
# print('test for a1p2, x=0.1', a1p2)
# a2p3 = param(0, 23, 3, 293, 0.101324)
# print('test for a2p3', a2p3)
# a2p3_highP = param(0.4, 23, 3, 850, 0.6)
# print('test for a2p3 high T and P', a2p3_highP)

#for all ranges
def SL_NH3_H2 (xh2, lam, temperature, pressure):
    xh2 = xh2
    lam = lam

```

```

temperature = temperature
pressure = pressure
Tn = temperature / 300
Pn = pressure / 0.101325

if (temperature <= 700) and (pressure <= 0.5) :
    if temperature <= 300:
        kappa2 = k1 * k2**Pn * Pn**k3 * lam**k4
    else: kappa2 = 1

def alpha_2(xh2, temperature, pressure):
    a2p3 = param(xh2, 23, 3, temperature, pressure)
    b2p3 = param(xh2, 27, 3, temperature, pressure)
    c2p3 = param(xh2, 31, 3, temperature, pressure)
    d2p3 = param(xh2, 35, 3, temperature, pressure)
    alpha_2f = a2p3 + b2p3*lam + c2p3*lam**2 + d2p3*lam**3
    return alpha_2f

def beta_2 (lam, xh2, temperature, pressure):
    a3p3 = param(xh2, 40, 3, temperature, pressure)
    b3p3 = param(xh2, 44, 3, temperature, pressure)
    c3p3 = param(xh2, 48, 3, temperature, pressure)
    beta_2f = a3p3 + b3p3*lam + c3p3/(lam**2)
    return beta_2f

def SLO2 (lam, xh2, temperature, pressure):
    a1p3 = param(xh2, 3, 3, temperature, pressure)
    b1p3 = param(xh2, 7, 3, temperature, pressure)
    c1p3 = param(xh2, 12, 3, temperature, pressure)
    d1p3 = param(xh2, 17, 3, temperature, pressure)
    SLO2f = (a1p3 + b1p3*lam) / (1 + c1p3*lam + d1p3*lam**2)
    return SLO2f

alpha_2f = alpha_2(xh2, temperature, pressure)

```

```

beta_2f = beta_2 (lam, xh2, temperature, pressure)
SLO2f = SLO2 (lam, xh2, temperature, pressure)
#print(f'alpha = {alpha_2f}, beta = {beta_2f}, SLO2 = {SLO2f}')

elif (700 < temperature <= 900) and (pressure <= 0.5) :
def alpha_2(xh2, temperature, pressure):
    a2p3 = param(xh2, 23, 3, temperature, pressure)
    b2p3 = param(xh2, 27, 3, temperature, pressure)
    c2p3 = param(xh2, 31, 3, temperature, pressure)
    d2p3 = param(xh2, 35, 3, temperature, pressure)
    alpha_2f = a2p3 + b2p3*lam + c2p3*lam**2 + d2p3*lam**3
    return alpha_2f

def beta_2 (lam, xh2, temperature, pressure):
    a3p3 = param(xh2, 40, 3, temperature, pressure)
    b3p3 = param(xh2, 44, 3, temperature, pressure)
    c3p3 = param(xh2, 48, 3, temperature, pressure)
    d3p3 = param(xh2, 52, 3, temperature, pressure)
    beta_2f = a3p3 + b3p3*lam + c3p3*(lam**2) + d3p3*(lam**3)
    return beta_2f

def SLO2 (lam, xh2, temperature, pressure):
    a1 = a10[1] / ((1 + np.exp(a11[1] - a12[1]*xh2)))**(1/a13[1])
    b1 = b10[1] / ((1 + np.exp(b11[1] - b12[1]*xh2)))**(1/b13[1])
    c1 = (c10[1] + c11[1]*xh2) / (1 + c12[1]*xh2 + c13[1]*(xh2**2))
    d1p4 = param(xh2, 17, 4, temperature, pressure)
    SLO2f = (a1 + b1*lam) / (1 + c1*lam + d1p4*lam**2)
    return SLO2f

#kappa2 = k1 * k2**Pn * Pn**k3 * lam**k4
kappa2 = 1

elif (temperature <= 800) and (pressure > 0.5) :
if temperature <= 300:
    kappa2 = k1 * k2**Pn * Pn**k3 * lam**k4

```

else: kappa2 = 1

def alpha_2(xh2, temperature, pressure):

a2p3 = param(xh2, 23, 3, temperature, pressure)

b2p3 = param(xh2, 27, 3, temperature, pressure)

c2p3 = param(xh2, 31, 3, temperature, pressure)

d2p3 = param(xh2, 35, 3, temperature, pressure)

alpha_2f = a2p3 + b2p3*lam + c2p3*lam**2 + d2p3*lam**3

return alpha_2f

def beta_2 (lam, xh2, temperature, pressure):

a3p2 = param(xh2, 40, 2, temperature, pressure)

b3p2 = param(xh2, 44, 2, temperature, pressure)

c3p2 = param(xh2, 48, 2, temperature, pressure)

d3p2 = param(xh2, 52, 2, temperature, pressure)

e3p2 = param(xh2, 56, 2, temperature, pressure)

beta_2f = a3p2 + b3p2*lam + c3p2*(lam**2) + d3p2*(lam**3) + e3p2*(lam**4)

return beta_2f

def SLO2 (lam, xh2, temperature, pressure):

a1 = a12[2]*(1 + a11[2]*xh2/a10[2])**(-1/a11[2])

b1p4 = param(xh2, 7, 4, temperature, pressure)

c1p3 = param(xh2, 12, 3, temperature, pressure)

d1p3 = param(xh2, 17, 3, temperature, pressure)

SLO2f = (a1 + b1p4*lam) / (1 + c1p3*lam + d1p3*(lam**2))

return SLO2f

elif (800 < temperature <= 1000) and (pressure > 0.5) :

def alpha_2(xh2, temperature, pressure):

a2p3 = param(xh2, 23, 3, temperature, pressure)

b2p3 = param(xh2, 27, 3, temperature, pressure)

c2p3 = param(xh2, 31, 3, temperature, pressure)

d2p3 = param(xh2, 35, 3, temperature, pressure)

alpha_2f = a2p3 + b2p3*lam + c2p3*lam**2 + d2p3*lam**3

return alpha_2f

```

def beta_2 (lam, xh2, temperature, pressure):
    a3p3 = param(xh2, 40, 3, temperature, pressure)
    b3p3 = param(xh2, 44, 3, temperature, pressure)
    c3p3 = param(xh2, 48, 3, temperature, pressure)
    beta_2f = a3p3 + b3p3*lam + c3p3*(lam**2)
    return beta_2f

def SLO2 (lam, xh2, temperature, pressure):
    a1 = a10[3] + (1-a10[3])*(1-np.exp(-a11[3]*xh2 - a12[3]*(xh2**2) - a13[3]*(xh2**3)))
    b1p4 = param(xh2, 7, 4, temperature, pressure)
    c1p4 = param(xh2, 12, 4, temperature, pressure)
    SLO2f = a1 * (b1p4**lam) * (lam**c1p4)
    return SLO2f

kappa2 = 1

SL_NH3_H2 = SLO2(lam, xh2, temperature, pressure) * (Tn**alpha_2(xh2, temperature, pressure)) *
(Pn**beta_2(lam, xh2, temperature, pressure)) * kappa2

print(kappa2)
return SL_NH3_H2
# -*- coding: utf-8 -*-
"""
Created on Thu May 18 13:12:36 2023

@author: esmot
"""

# NH3/H2/N2/Air Mixture Laminar Burning Velocities
# P is in MPa
# T is in K
# returns LBV in m/s, cm/s in the plots

```

```
import numpy as np
import math
import pandas as pd
from decimal import Decimal, getcontext
import matplotlib.pyplot as plt

co = pd.read_excel(r'Correlation_Coefficients.xlsx')

coeff = np.array(co, dtype=Decimal)

a10_1 = coeff[3,1:5]
a11_1 = coeff[4,1:5]
a12_1 = coeff[5,1:5]
a13_1 = coeff[6,1:5]
b10_1 = coeff[7,1:5]
b11_1 = coeff[8,1:5]
b12_1 = coeff[9,1:5]
b13_1 = coeff[10,1:5]
b14_1 = coeff[11,1:5]
c10_1 = coeff[12,1:5]
c11_1 = coeff[13,1:5]
c12_1 = coeff[14,1:5]
c13_1 = coeff[15,1:5]
c14_1 = coeff[16,1:5]
d10_1 = coeff[17,1:5]
d11_1 = coeff[18,1:5]
d12_1 = coeff[19,1:5]
d13_1 = coeff[20,1:5]
d14_1 = coeff[21,1:5]
a20_1 = coeff[23,1:5]
a21_1 = coeff[24,1:5]
a22_1 = coeff[25,1:5]
a23_1 = coeff[26,1:5]
b20_1 = coeff[27,1:5]
```

b21_1 = coeff[28,1:5]
b22_1 = coeff[29,1:5]
b23_1 = coeff[30,1:5]
c20_1 = coeff[31,1:5]
c21_1 = coeff[32,1:5]
c22_1 = coeff[33,1:5]
c23_1 = coeff[34,1:5]
d20_1 = coeff[35,1:5]
d21_1 = coeff[36,1:5]
d22_1 = coeff[37,1:5]
d23_1 = coeff[38,1:5]
a30_1 = coeff[40,1:5]
a31_1 = coeff[41,1:5]
a32_1 = coeff[42,1:5]
a33_1 = coeff[41,1:5]
b30_1 = coeff[44,1:5]
b31_1 = coeff[45,1:5]
b32_1 = coeff[46,1:5]
b33_1 = coeff[47,1:5]
c30_1 = coeff[48,1:5]
c31_1 = coeff[49,1:5]
c32_1 = coeff[50,1:5]
c33_1 = coeff[51,1:5]
d30_1 = coeff[52,1:5]
d31_1 = coeff[53,1:5]
d32_1 = coeff[54,1:5]
d33_1 = coeff[55,1:5]
_e30 = coeff[56,1:5]
_e31 = coeff[57,1:5]
_e32 = coeff[58,1:5]
k1 = coeff[60,1]
k2 = coeff[61,1]
k3 = coeff[62,1]
k4 = coeff[63,1]

```
def param(xh2, l_row, p_index, temperature, pressure):
```

```
    qkn = 0
```

```
    if (temperature <= 700) and (pressure <= 0.5):
```

```
        if xh2 == 0:
```

```
            qkn = coeff[l_row,1]
```

```
        else:
```

```
            for i in range (0, p_index+1):
```

```
                qkn += coeff[l_row+i,1] * xh2**i
```

```
            #print(qkn)
```

```
    elif (temperature > 700) and (pressure <= 0.5):
```

```
        if xh2 == 0:
```

```
            qkn = coeff[l_row,2]
```

```
        else:
```

```
            for i in range (0, p_index+1):
```

```
                qkn += coeff[l_row+i,2] * xh2**i
```

```
            #print(qkn)
```

```
    elif (temperature <= 800) and (pressure > 0.5):
```

```
        if xh2 == 0:
```

```
            qkn = coeff[l_row,3]
```

```
        else:
```

```
            for i in range (0, p_index+1):
```

```
                qkn += coeff[l_row+i,3] * xh2**i
```

```
            #print(qkn)
```

```
    elif (temperature > 800) and (pressure > 0.5):
```

```
        if xh2 == 0:
```

```
            qkn = coeff[l_row,4]
```

```
        else:
```

```

        for i in range (0, p_index+1):
            qkn += coeff[l_row+i,4] * xh2**i
            #print(qkn)
    else:
        print('Invalid temperature and pressure specified')

    #print(qkn)
    return qkn

co2 = pd.read_excel(r'Correlation_Coefficients_NH3_H2_N2.xlsx')

coeff2 = np.array(co2)#, dtype=Decimal)

a = coeff2[1,1:5]
b = coeff2[2,1:5]
c = coeff2[3,1:5]

d0 = coeff2[5,1:5]
d1 = coeff2[6,1:5]
d2 = coeff2[7,1:5]
d3 = coeff2[8,1:5]

d01 = coeff2[10,1:5]
d02 = coeff2[11,1:5]
d03 = coeff2[12,1:5]
d04 = coeff2[13,1:5]

d10 = coeff2[15,1:5]
d11 = coeff2[16,1:5]
d12 = coeff2[17,1:5]
d13 = coeff2[18,1:5]
d14 = coeff2[19,1:5]

```

```
d20 = coeff2[21,1:5]
d21 = coeff2[22,1:5]
d22 = coeff2[23,1:5]
d23 = coeff2[24,1:5]
d24 = coeff2[25,1:5]
d25 = coeff2[26,1:5]
```

```
e = coeff2[28,1:5]
```

```
e0 = coeff2[30,1:5]
e1 = coeff2[31,1:5]
e2 = coeff2[32,1:5]
e3 = coeff2[33,1:5]
```

```
f0 = coeff2[35,1:5]
f1 = coeff2[36,1:5]
f2 = coeff2[37,1:5]
f3 = coeff2[38,1:5]
```

```
g = coeff2[40,1:5]
```

```
h0 = coeff2[42,1:5]
h1 = coeff2[43,1:5]
h2 = coeff2[44,1:5]
h3 = coeff2[45,1:5]
```

```
def LBV(xh2, lam, temperature, pressure):
```

```
    z = xh2 / 3
```

```
    #print(z)
```

```
    Tn = temperature / 300
```

```
    Pn = pressure / 0.101325
```

if (pressure <= 0.5) and (temperature <= 700):

```
def alpha_2(xh2, temperature, pressure):  
    a2p3 = param(xh2, 23, 3, temperature, pressure)  
    b2p3 = param(xh2, 27, 3, temperature, pressure)  
    c2p3 = param(xh2, 31, 3, temperature, pressure)  
    d2p3 = param(xh2, 35, 3, temperature, pressure)  
    alpha_2f = a2p3 + b2p3*lam + c2p3*lam**2 + d2p3*lam**3  
    return alpha_2f
```

```
def beta_2 (lam, xh2, temperature, pressure):  
    a3p3 = param(xh2, 40, 3, temperature, pressure)  
    b3p3 = param(xh2, 44, 3, temperature, pressure)  
    c3p3 = param(xh2, 48, 3, temperature, pressure)  
    beta_2f = a3p3 + b3p3*lam + c3p3/(lam**2)  
    return beta_2f
```

```
def gamma(xh2, lam, temperature, pressure):  
    h = h0[0] + h1[0]*z + h2[0]*(z**2) + h3[0]*(z**3)  
    d = d0[0] + d1[0]*z + d2[0]*(z**2)  
    f = f0[0] + f1[0]*z + f2[0]*(z**2) + f3[0]*(z**3)  
    gamma1 = (a[0] + b[0]*Tn + c[0]*(Tn**2)) * (Pn**g[0]) * lam**h * d*(xh2-e[0])**f  
    return gamma
```

```
def SLO2 (lam, xh2, temperature, pressure):  
    a1p3 = param(xh2, 3, 3, temperature, pressure)  
    b1p3 = param(xh2, 7, 3, temperature, pressure)  
    c1p3 = param(xh2, 12, 3, temperature, pressure)  
    d1p3 = param(xh2, 17, 3, temperature, pressure)  
    SLO2f = (a1p3 + b1p3*lam) / (1 + c1p3*lam + d1p3*lam**2)  
    return SLO2f
```

elif (pressure <= 0.5) and (700 < temperature <= 900):

```
def alpha_2(xh2, temperature, pressure):  
    a2p3 = param(xh2, 23, 3, temperature, pressure)
```

```

b2p3 = param(xh2, 27, 3, temperature, pressure)
c2p3 = param(xh2, 31, 3, temperature, pressure)
d2p3 = param(xh2, 35, 3, temperature, pressure)
alpha_2f = a2p3 + b2p3*lam + c2p3*lam**2 + d2p3*lam**3
return alpha_2f

```

```

def beta_2 (lam, xh2, temperature, pressure):
    a3p3 = param(xh2, 40, 3, temperature, pressure)
    b3p3 = param(xh2, 44, 3, temperature, pressure)
    c3p3 = param(xh2, 48, 3, temperature, pressure)
    d3p3 = param(xh2, 52, 3, temperature, pressure)
    beta_2f = a3p3 + b3p3*lam + c3p3*(lam**2) + d3p3*(lam**3)
    return beta_2f

```

```

def SLO2 (lam, xh2, temperature, pressure):
    a1 = a10_1[1] / ((1 + np.exp(a11_1[1] - a12_1[1]*xh2))**(1/a13_1[1]))
    b1 = b10_1[1] / ((1 + np.exp(b11_1[1] - b12_1[1]*xh2))**(1/b13_1[1]))
    c1 = (c10_1[1] + c11_1[1]*xh2) / (1 + c12_1[1]*xh2 + c13_1[1]*(xh2**2))
    d1p4 = param(xh2, 17, 4, temperature, pressure)
    SLO2f = (a1 + b1*lam) / (1 + c1*lam + d1p4*lam**2)
    return SLO2f

```

```

def gamma(xh2, lam, temperature, pressure):
    h = h0[1] + h1[1]*z + h2[1]*(z**2) + h3[1]*(z**3)
    d = (d0[1] + d1[1]*z) / (1 + d2[1]*z + d3[1]*(z**2))
    e_ = 1 / (e0[1] + e1[1]*z)
    f = f0[1] + f1[1]*z + f2[1]*(z**2) + f3[1]*(z**3)
    gamma = (a[1] + b[1]*Tn + c[1]*(Tn**2)) * (Pn**g[1]) * (lam**h) * d*(xh2-e_)**f
    return gamma

```

```

elif (pressure > 0.5) and (temperature <= 800):

```

```

    def alpha_2(xh2, temperature, pressure):
        a2p3 = param(xh2, 23, 3, temperature, pressure)
        b2p3 = param(xh2, 27, 3, temperature, pressure)

```

```

c2p3 = param(xh2, 31, 3, temperature, pressure)
d2p3 = param(xh2, 35, 3, temperature, pressure)
alpha_2f = a2p3 + b2p3*lam + c2p3*lam**2 + d2p3*lam**3
return alpha_2f

```

```

def beta_2 (lam, xh2, temperature, pressure):
    a3p2 = param(xh2, 40, 2, temperature, pressure)
    b3p2 = param(xh2, 44, 2, temperature, pressure)
    c3p2 = param(xh2, 48, 2, temperature, pressure)
    d3p2 = param(xh2, 52, 2, temperature, pressure)
    e3p2 = param(xh2, 56, 2, temperature, pressure)
    beta_2f = a3p2 + b3p2*lam + c3p2*(lam**2) + d3p2*(lam**3) + e3p2*(lam**4)
    return beta_2f

```

```

def SLO2 (lam, xh2, temperature, pressure):
    a1 = a12_1[2]*(1+ a11_1[2]*xh2/a10_1[2])**(-1/a11_1[2])
    b1p4 = param(xh2, 7, 4, temperature, pressure)
    c1p3 = param(xh2, 12, 3, temperature, pressure)
    d1p3 = param(xh2, 17, 3, temperature, pressure)
    SLO2f = (a1 + b1p4*lam) / (1 + c1p3*lam + d1p3*(lam**2))
    return SLO2f

```

```

def gamma(xh2, lam, temperature, pressure):
    h = h0[2] + h1[2]*z + h2[2]*(z**2) + h3[2]*(z**3)
    d0_ = d01[2] / (1 + np.exp(d02[2] - d03[2]*z))
    d1_ = (d10[2]*d11[2] + d12[2]*(z**d13[2])) / (d11[2] + (z**d13[2]))
    d2_ = d20[2] + d21[2]*z + d22[2]*(z**2) + d23[2]*(z**3) + d24[2]*(z**4) + d25[2]*(z**5)
    d_ = d0_ * np.exp(-z/d1_ + d2_)
    e_ = (e0[2] + e1[2]*z) / (1 + e2[2]*z + e3[2]*(z**2))
    f = (f0[2] + f1[2]*z) / (1 + f2[2]*z + f3[2]*(z**2))
    gamma = (a[2] + b[2]*Tn + c[2]*(Tn**2)) * (Pn**g[2]) * lam**h * d_*(xh2-e_)**f
    return gamma

```

```

elif (pressure > 0.5) and (800 < temperature <= 1000):

```

```

def alpha_2(xh2, temperature, pressure):
    a2p3 = param(xh2, 23, 3, temperature, pressure)
    b2p3 = param(xh2, 27, 3, temperature, pressure)
    c2p3 = param(xh2, 31, 3, temperature, pressure)
    d2p3 = param(xh2, 35, 3, temperature, pressure)
    alpha_2f = a2p3 + b2p3*lam + c2p3*lam**2 + d2p3*lam**3
    return alpha_2f

def beta_2 (lam, xh2, temperature, pressure):
    a3p3 = param(xh2, 40, 3, temperature, pressure)
    b3p3 = param(xh2, 44, 3, temperature, pressure)
    c3p3 = param(xh2, 48, 3, temperature, pressure)
    beta_2f = a3p3 + b3p3*lam + c3p3*(lam**2)
    return beta_2f

def SLO2 (lam, xh2, temperature, pressure):
    a1 = a10_1[3] + (1-a10_1[3])*(1-np.exp(-a11_1[3]*xh2 - a12_1[3]*(xh2**2) -
a13_1[3]*(xh2**3)))
    b1p4 = param(xh2, 7, 4, temperature, pressure)
    c1p4 = param(xh2, 12, 4, temperature, pressure)
    SLO2f = a1 * (b1p4**lam) * (lam**c1p4)
    return SLO2f

def gamma(xh2, lam, temperature, pressure):
    h = h0[3] + h1[3]*z + h2[3]*(z**2) + h3[3]*(z**3)
    #d0_ = d01[3] + (d02[3])*z + d03[3]*(z**2) + d04[3]*(z**3)
    d0_ = 0.170238 + -2.814798*z + 22.571051*(z**2) + 32.836779*(z**3)
    d1_ = d10[3] + (1-d10[3])*(1 - np.exp(-d11[3]*z - d12[3]*(z**2) - d13[3]*(z**3) -
d14[3]*(z**4)))
    d2_ = d20[3] + (1-d20[3])*(1 - np.exp(-d21[3]*z - d22[3]*(z**2) - d23[3]*(z**3) -
d24[3]*(z**4)))
    d_ = d0_ * np.exp(-z/d1_ + d2_)
    e_ = (e0[3]*e1[3] + e2[3]*(z**e3[3])) / (e1[3] + z**e3[3])
    f = (f0[3] + f1[3]*z) / (1 + f2[3]*z + f3[3]*(z**2))

```

```

    gamma = (a[3] + b[3]*Tn + c[3]*(Tn**2)) * (Pn**g[3]) * lam**h * d_*(xh2-e_)**f
    return gamma
else:
    print('invalid temperature, pressure, xh2 or xn2 specified')

SL = (SLO2(lam, xh2, temperature, pressure)) * gamma(xh2, lam, temperature, pressure) *
Tn**(alpha_2(xh2, temperature, pressure)) * Pn**(beta_2(lam, xh2, temperature, pressure))
print('gamma is', gamma)

return SL

```

APPENDIX D PERMISSIONS

Permissions from publishers to include Figures 1.1 – 1.9, 1.11, 2.2 – 2.4, and Tables 1.1 – 1.2 can be found in the Supplemental File: [StatementsofPermissionsGolonski.docx](#).